JOURNAL OF GEOPHYSICAL RESEARCH, VOL. 101, NO. D6, PAGES 9957–9982, APRIL 30, 1996

Calibration of the Microwave Limb Sounder on the Upper Atmosphere Research Satellite

R.F. Jarnot, R.E. Cofield, J.W. Waters, and D.A. Flower
Jet Propulsion Laboratory, California Institute of Technology, Pasadena

G.E. Peckham
Physics Department, Heriot-Watt University, Edinburgh, Scotland

Abstract. The Microwave Limb Sounder (MLS) is a three-radiometer, passive, limb emission instrument onboard the Upper Atmosphere Research Satellite (UARS). Radiometric, spectral and field-of-view calibrations of the MLS instrument are described in this paper. In-orbit noise performance, gain stability, spectral baseline and dynamic range are described, as well as use of in-flight data for validation and refinement of prelaunch calibrations. Estimated systematic scaling uncertainties (3σ) on calibrated limb radiances from prelaunch calibrations are 2.6% in bands 1 through 3, 3.4% in band 4, and 6% in band 5. The observed systematic errors in band 6 are ~15%, consistent with prelaunch calibration uncertainties. Random uncertainties on individual limb radiance measurements are very close to the levels predicted from measured radiometer noise temperature, with negligible contribution from noise and drifts on the regular in-flight gain calibration measurements.

Introduction

The Microwave Limb Sounder onboard NASA's Upper Atmosphere Research Satellite is the first implementation of atmospheric limb sounding from space using microwaves. It was launched on September 12, 1991, with useful measurements starting within 1 week of launch, becoming fully operational within 2 weeks. The MLS is a passive instrument sensing thermal emission in 6 mm-wavelength spectral bands with radiometers centered near 63, 183 and 205 GHz. Primary measurements are stratospheric profiles of ClO, O_3, H_2O, temperature, and field-of-view (FOV) tangent point pressure which provides the pointing reference for retrievals of the other geophysical quantities. Additional products include stratospheric HNO_3, volcanically enhanced SO_2, geopotential height, and upper tropospheric H_2O. Data are routinely analyzed and processed to produce daily maps of all retrieved quantities within 2 days of data acquisition.

This paper describes the generation of calibrated limb radiances from raw instrument data, postlaunch analyses of instrument performance, as well as the prelaunch determination of instrument characteristics used in the retrieval of geophysical parameter profiles from the limb radiances. Appendix A summarizes the notation used in our equations. Details not covered here are given in the MLS Calibration Report [*Jarnot and Cofield*, 1991]. References which describe the general technique of microwave remote sensing include *Staelin* [1969], *Njoku* [1982], *Ulaby et al.* [1981, 1986] and *Janssen* [1993].

Paper number 95JD03792.
0148-0227/96/95JD-03792$05.00

Instrument

The MLS instrument is described by *Barath et al.* [1993] and the microwave limb sounding measurement technique by *Waters* [1993]. Figure 1 is a block diagram of the instrument, and Table 1 lists its spectral bands and primary measurements. In-flight radiometric calibration is performed by the switching mirror which directs the FOVs of all radiometers simultaneously to one of three sources: the limb port (L), which accepts radiation from the antenna (A), the space port (S), which views the "cold" space reference, and the calibration target port (T), which views an ambient temperature blackbody target.

The MLS down-converts signals in 6 bands (B1–B6) to a common center frequency of 400 MHz for analysis by nominally identical 15-channel filter banks, each of ~500-MHz bandwidth. The three radiometers (R1–R3) operate nonswitched during individual measurements, and their FOVs vertically step-scan the atmospheric limb every 65.536 s, the MLS major frame (MMAF), as shown in Table 2. An MMAF is comprised of 32 MLS minor frames (MMIF), each of duration 2.048 s. The first 1.728 s of each MMIF is used for signal integration and digitization, the remaining time being available for movement of the antenna and/or switching mirror. The signal integration time is programmable and was set to 1.792 s for the first year of operation (until September 25, 1992), after which the slight decrease in spacecraft minimum orbital bus voltage due to battery aging

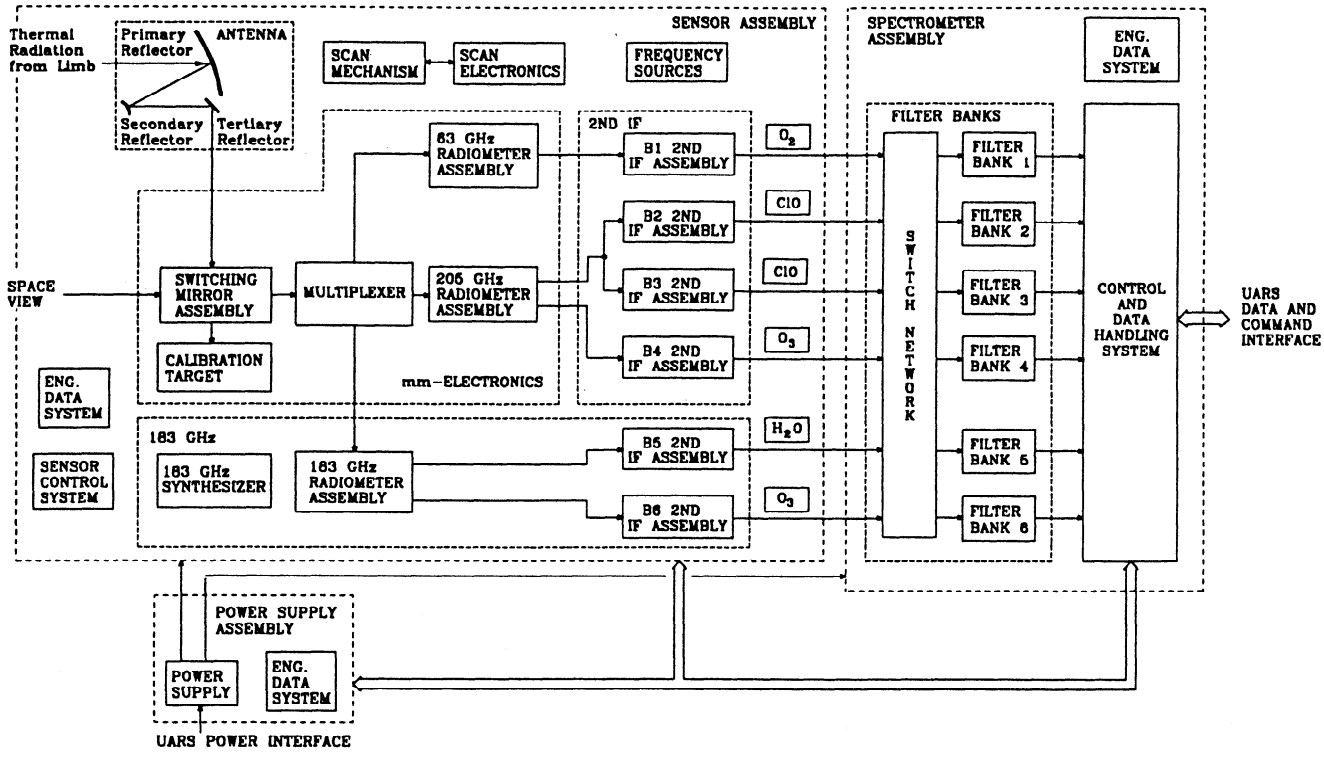

Figure 1. Block diagram of UARS MLS. The switching mirror routes signals from the scanning antenna, space, and target ports to the radiometers via a quasi-optical multiplexer. The intermediate frequency (IF) switch network provides spectrometer redundancy for the most important bands. The filter bank spectrometers each have 15 channels and are nominally identical.

prevented all movements of the MLS switching mirror from being completed in the interval between data integrations. The 64-ms reduction in integration time has negligible effect on signal to noise (S/N) of the science data, but the additional 64 ms for step and settle has proven sufficient to accommodate any further aging of both the spacecraft batteries and the switching mirror motor bearings. All measurements are made simultaneously and continuously, and the bands are analyzed by the filter bank spectrometers which have channel widths ranging progressively from 2 MHz at band center to 128 MHz at band edges, providing variable resolution to track broadening spectral features as the FOV scans down from ~90-km tangent height to just above the ground.

Table 1. MLS Spectral Bands and Primary Measurements

Radiometer	Band	Frequency, GHz	Measurement
R1	B1	63.283	P, T
R2	B2/B3	204.352	ClO
R2	B4	206.132	O_3
R3	B5	183.310	H_2O
R3	B6	184.378	O_3

Frequency indicated is that of the center of the passband in the signal sideband, except for band 1, for which the first LO frequency is given. The three radiometers are referred to as R1–R3 in the text, and the six bands as B1–B6. P and T are pressure and temperature.

Calibration

MLS data processing is partitioned into three "Levels", the first two being *Level 1:* converts the raw instrument data into daily files of calibrated limb radiances, together with corresponding estimates of their precision, and daily files of calibrated engineering data; collates ancillary data required by Level 2 processing into the daily Level 1 output files; and *Level 2:* retrieves geophysical parameter profiles using the Level 1 radiance files.

Both Level 1 and Level 2 processing software require prelaunch calibration data. Level 1 requires knowledge of calibration target emissivity and temperature and of optical properties of all elements in the paths between the switching mirror and the ambient calibration target, the space port and the Earth's limb. Tables of partial derivatives used in Level 2 (*W.G. Read et al.*, manuscript in preparation, 1996) require detailed knowledge of individual channel spectral responses and antenna FOV angular and polarization responses.

This paper proceeds with a brief description of instrument operation, followed by descriptions of routine in-flight radiometric calibration algorithms, and additional calibrations in the following categories: *radiometric,* ab-

Table 2. Nominal In-Flight Scan and Calibration Sequence for each MLS Major Frame (MMAF)

Minor Frame	Step Angle	Motor Steps	Nominal Tangent Height/km	View
0	0.0000°	0	90.0	L
1	-0.1300°	52	83.9	L
2	-0.1275°	51	77.8	L
3	-0.1275°	51	71.8	L
4	-0.1275°	51	65.8	L
5	-0.1275°	51	59.8	L
6	-0.1275°	51	53.7	L
7	-0.0850°	34	49.7	S
8	0.0000°	0	49.7	L
9	-0.0850°	34	45.7	L
10	-0.0850°	34	41.7	L
11	-0.0650°	26	38.6	L
12	-0.0650°	26	35.6	L
13	-0.0625°	25	32.6	L
14	-0.0650°	25	29.7	L
15	-0.0625°	25	26.7	S
16	0.0000°	0	26.7	L
17	-0.0500°	20	24.3	L
18	-0.0300°	12	22.9	L
19	-0.0300°	12	21.5	L
20	-0.0300°	12	20.0	L
21	-0.0300°	12	18.7	L
22	-0.0300°	12	17.3	L
23	-0.0450°	18	15.1	S
24	0.0000°	0	15.1	L
25	-0.0450°	18	13.0	L
26	-0.0675°	27	9.8	L
27	-0.0675°	27	6.6	L
28	-0.0750°	30	3.1	L
29	0.0000°	0	3.1	S
30		Antenna retrace		T
31		Antenna retrace		S

The step angle is the vertical displacement of the FOV boresight during each step. This sequence repeats every 65.536 s. L, S, and T indicate that the switching mirror is viewing the limb, space, or calibration target ports, respectively. At Level 2 the MMIF sequence within an MMAF is labeled from 1 to 32. This difference should be noted when comparing information presented here with that in the UARS MLS data validation papers.

solute response of the instrument as a function of input signal power; *spectral,* relative response as a function of frequency; *field-of-view,* relative response as a function of angle and polarization; *engineering,* knowledge of the internal references used for determining MLS voltages, currents, and temperatures. An important aspect of the MLS calibration philosophy was to perform end-to-end calibrations wherever possible.

Heterodyne Radiometers and Blackbody Radiation

The MLS radiometers are heterodyne systems which receive power $h\nu/\{\exp(h\nu/kT)-1\}$ per unit frequency range when viewing a blackbody source at temperature T which completely fills their FOV, where ν is frequency, h is Planck's constant, and k is Boltzmann's constant (see Appendix B). The MLS signals originate thermally, and it is convenient to measure radiant power per unit bandwidth, $\dot{P}_\nu$, in units of temperature so that the measure converges to the absolute temperature, T, in the long wave (Rayleigh-Jeans) limit where $h\nu \ll kT$ and classical statistical mechanics applies. For the blackbody this is

$$\dot{P}_\nu^{BB} = \frac{h\nu}{k\{\exp(h\nu/kT)-1\}} \tag{1}$$

The long wave expansion of this expression and values (in Kelvin) of the individual terms for various temperatures are given below for $\nu = 205$ GHz, approximately the highest frequency received by UARS MLS.

$$\begin{array}{rcrcrcl} \dot{P}_\nu^{BB} & = & T & - & \frac{h\nu}{2k} & + & \left(\frac{h\nu}{2k}\right)^2 \frac{1}{3T} \quad \cdots \\ 295.107 & = & 300 & - & 4.919 & + & 0.027 \quad \cdots \\ 95.161 & = & 100 & - & 4.919 & + & 0.081 \quad \cdots \\ 0.264 & = & 2.7 & - & 4.919 & + & 2.988 \quad \cdots \end{array} \tag{2}$$

Temperatures of the atmospheric regions measured by the MLS and of its internal calibration target are within the 150 to 300-K range, for which $\dot{P}_\nu^{BB} \approx T+\delta T$, where δT is a small, nearly temperature independent, offset. The full formula (1) is used throughout processing of MLS data.

Radiometric Response

The response of radiometer channel i is proportional to received power $\dot{P}_i^{MX}$ obtained by integrating the power per unit frequency and per unit solid angle, $\dot{I}_\nu^{MX}(\theta,\phi)$, incident on the switching mirror (M) from view X over angle and frequency with weighting functions $G^M(\nu,\theta,\phi)$ and $F_i(\nu)$ which describe the angular and frequency response of the antenna and radiometer respectively:

$$\dot{P}_i^{MX} = \frac{1}{4\pi}\int_\nu\int_\Omega \dot{I}_\nu^{MX}(\theta,\phi)F_i(\nu)G^M(\nu,\theta,\phi)\,d\Omega\,d\nu \tag{3}$$

where $F_i(\nu)$ is normalized to unit area ($\int_\nu F_i(\nu)d\nu = 1$), $\int_\Omega G d\Omega = 4\pi$ (Appendix B), and the integrals are evaluated over the full range of frequencies and solid angles over which the instrument has a response.

The following considerations are important in relating the radiation incident upon the switching mirror to that from the antenna, target, and space:

1. The views from the switching mirror are restricted by baffles, coated with absorbing paint, which define solid angles Ω_{MX} for view X. We define quantities $\dot{P}_i^X$ for $X = L$, T, or S from (3) by restricting the integral to the solid angle Ω_{MX}:

$$\dot{P}_i^X = \frac{\displaystyle\int_\nu\int_{\Omega_{MX}} \dot{I}_\nu^X(\theta,\phi)F_i(\nu)G_r^M(\theta,\phi)\,d\Omega\,d\nu}{\displaystyle\int_{\Omega_{MX}} G_r^M(\theta,\phi)\,d\Omega} \tag{4}$$

($\dot{I}_\nu^{MX} \equiv \dot{I}_\nu^X$ for directions within solid angle Ω_{MX})

2. The variation of $G^M(\nu,\theta,\phi)$ is small across the range of frequencies accepted by any one radiometer

which allows it to be replaced by $G_r^M(\theta,\phi)$, its value near the center frequency, ν_r, of radiometer r in (4) above.

3. Radiation $\dot{I}_\nu^X$ from the calibration target and from space is isotropic and has a blackbody spectrum.

With the above approximations, for the limb view,

$$\dot{P}_i^{ML} = \eta_r^{ML}\dot{P}_i^L + (1-\eta_r^{ML})\dot{P}_r^{BL} \tag{5}$$

where $\eta_r^{ML} = \frac{1}{4\pi}\int_{\Omega_{ML}} G_r^M(\theta,\phi)\,d\Omega$, and $\dot{P}_r^{BL}$ is the radiation from the baffle in the limb view, averaged over the solid angle outside Ω_{ML}. Similarly, for the target ($X = T$) and space ($X = S$) views,

$$\dot{P}_i^{MX} = \eta_r^{MX}\dot{P}_r^X + (1-\eta_r^{MX})\dot{P}_r^{BX} \tag{6}$$

where η_r^{MX} and $\dot{P}_r^{BX}$ are the corresponding values for these two views, and $\dot{P}_r^X = \dot{P}_{\nu_r}^X$.

Antenna Effects

The antenna, interposed between the switching mirror and the atmospheric limb, transforms the FOV of the radiometer so that when calculating $\dot{P}_i^A$ from $\dot{I}_\nu^L(\theta,\phi)$, $G_r^M(\theta,\phi)$ must be replaced by $G_r^A(\theta,\phi)$, the measured antenna gain. Imperfections in the antenna and practical limitations on its characterization result in the introduction of further terms. One limitation is that $G_r^A(\theta,\phi)$ can be measured only over directions included in a solid angle Ω_A (about $\pm 6°$ from the boresight axis). The calculated response for directions outside this range and the calculated ohmic loss in the antenna are used to estimate an effective transmission loss of the radiation from the limb and an additive radiation offset from the antenna.

Antenna transmission is more easily described by considering the antenna as a transmitter with illumination function $G_r^M(\theta,\phi)$ (restricted to solid angle Ω_{ML}). Two processes are involved: (1) ohmic loss: the antenna transmission due to ohmic loss is ρ_r^A where a fraction $(1-\rho_r^A)$ of the incident radiation is absorbed; (2) diffraction and scattering: of the remainder, a fraction $(1-\eta_r^A)$ is transmitted into directions outside the solid angle Ω_A over which the antenna pattern is characterized in detail. This is accounted for by introducing an efficiency η_r^A, where

$$\eta_r^A = \frac{1}{4\pi}\int_{\Omega_A} G_r^A(\theta,\phi)\,d\Omega \tag{7}$$

Radiation offsets arise from the same two processes: (1) ohmic loss: radiation $(1-\rho_r^A)\dot{P}_r^{OA}$ is emitted by the antenna, where $\dot{P}_r^{OA}$ is an effective brightness for the antenna thermal emission; (2) diffraction and scattering: radiation $(1-\eta_r^A)\rho_r^A\dot{P}_r^{SA}$, characterized by an effective brightness $\dot{P}_r^{SA}$, is scattered outside solid angle Ω_A.

Calculated values of $\dot{P}_i^L$ ($\equiv \dot{P}_i^L$) are produced for Level 2 processing (*W.G. Read et. al.*, in preparation, 1996) by integrating $\dot{I}_\nu^A(\theta,\phi)$ over the angular response of the antenna within solid angle Ω_A and over the frequency response of a radiometer channel, where

$$\dot{P}_i^L = \frac{\int_\nu\int_{\Omega_A} \dot{I}_\nu^A(\theta,\phi)F_i(\nu)G_r^A(\theta,\phi)\,d\Omega\,d\nu}{\int_{\Omega_A} G_r^A(\theta,\phi)\,d\Omega} \tag{8}$$

One objective of MLS Level 1 processing is to produce measured values of $\dot{P}_i^L$ for use in Level 2 processing. Accounting for loss and scattering, as described above, relates $\dot{P}_i^L$ to the signal emerging from the switching mirror when viewing the antenna:

$$\dot{P}_i^A = \rho_r^A\eta_r^A\dot{P}_i^L + (1-\rho_r^A)\dot{P}_r^{OA} + (1-\eta_r^A)\rho_r^A\dot{P}_r^{SA} \tag{9}$$

In-Flight Radiometric Calibration Algorithms

In-flight radiometric calibration is performed during every limb scan using the switching mirror to direct the FOVs of all radiometers to the space and internal calibration target ports. The MLS scanning and switching sequence which has been used for most of the mission is shown in Table 2. The filter bank detectors are operated at sufficiently low signal power to provide a linear relationship between input radiance and channel output, as illustrated in Figure 2, where the abscissa indicates signal power collected by the switching mirror, and the ordinate indicates the output counts from the voltage-to-frequency (V/F) converter digitizer of channel i.

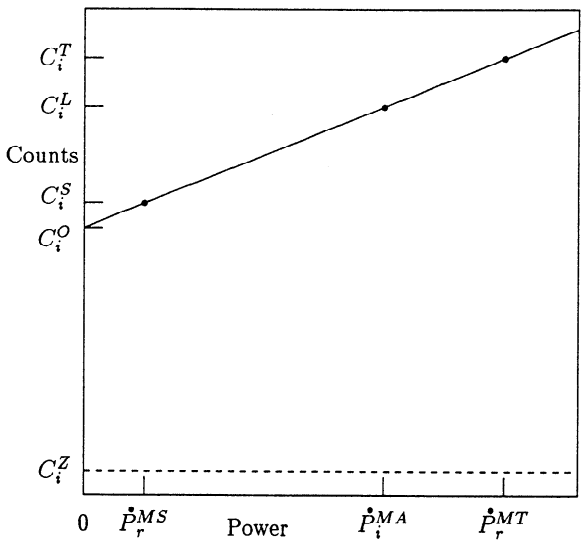

Figure 2. Plot illustrating the linear relationship between filter bank channel digitized output (counts) and power collected by the switching mirror. S, A and T correspond to the space, limb (antenna) and target views of the switching mirror, respectively. C_i^O is the offset generated by instrument noise and C_i^Z is the offset built into the digitizing system.

In the absence of noise or drifts, the output of channel i for each of the three switching mirror positions is given by

$$\begin{aligned} C_i^L &= g_i\left(\eta_r^{ML}\dot{P}_i^A + (1-\eta_r^{ML})\dot{P}_r^{BL}\right) + C_i^O, \\ C_i^T &= g_i\left(\eta_r^{MT}\dot{P}_r^T + (1-\eta_r^{MT})\dot{P}_r^{BT}\right) + C_i^O, \\ C_i^S &= g_i\left(\eta_r^{MS}\dot{P}_r^S + (1-\eta_r^{MS})\dot{P}_r^{BS}\right) + C_i^O. \end{aligned} \quad (10)$$

where C_i^X are the outputs of channel i for the three switching mirror positions X, C_i^Z, and C_i^O are offsets (Figure 2), described below, and g_i is the overall radiometric gain of channel i (expressed in counts per Kelvin of signal brightness). C_i^Z represents the output counts from the digitizer of channel i with no signal input to the filter bank, C_i^O the hypothetical output counts if the radiometers were to view a source of zero brightness, and the other terms have been defined earlier. The count difference between C_i^O and C_i^Z is generated by radiometer noise characterized by a system temperature, T_{sys}, which is routinely computed (converted to units of Kelvin) by Level 1 software as a diagnostic of radiometer performance.

Level 1 Calibration Algorithms

Routine in-flight gain calibration is computed from measurements performed every MMAF by rotating the switching mirror so that the FOVs of all radiometers are directed toward an internal ambient target for one MMIF and to the space port for five other MMIFs distributed through each MMAF (see Table 2).

Channel gain at the time of the target view, $\hat{g}_i(T)$, is estimated by

$$\hat{g}_i(T) = \frac{C_i^T - \widehat{C}_i^S(T)}{\left(\eta_r^{MT}\dot{P}_r^T - \eta_r^{MS}\dot{P}_r^S + (1-\eta_r^{MT})\dot{P}_r^{BT} - (1-\eta_r^{MS})\dot{P}_r^{BS}\right)} \quad (11)$$

where the "radiation offset" terms in the denominator involving $\dot{P}_r^{BT}$ and $\dot{P}_r^{BS}$ are provided from FOV calibrations discussed below. The estimated space reference counts at the time of the target view, $\widehat{C}_i^S(T)$, are provided by interpolation via a quadratic fit to space views taken over an 11 MMAF window centered about the target frame. The estimate of gain at the time of each limb view, $\hat{g}_i(L)$, is then obtained by interpolation via a quadratic fit to $\hat{g}_i(T)$ over 11 MMAFs centered at the time of the limb view. Solving the first and third of equations (10) for $\dot{P}_i^A$, and using $\hat{g}_i(L)$ for g_i, gives

$$\dot{P}_i^A = \frac{1}{\eta_r^{ML}}\left(\frac{C_i^L - \widehat{C}_i^S(L)}{\hat{g}_i(L)} + \eta_r^{MS}\dot{P}_r^S - (1-\eta_r^{ML})\dot{P}_r^{BL} + (1-\eta_r^{MS})\dot{P}_r^{BS}\right) \quad (12)$$

where $\widehat{C}_i^S(L)$ is the interpolated value of the space counts at the time of the limb view, obtained using an 11 MMAF window and quadratic fit as for the gain interpolation. The limb radiance obtained from (9) is

$$\dot{P}_i^L = \frac{1}{\eta_r^A \rho_r^A}\left(\dot{P}_i^A - (1-\rho_r^A)\dot{P}_r^{OA} - (1-\eta_r^A)\rho_r^A \dot{P}_r^{SA}\right) \quad (13)$$

where (12) is used for $\dot{P}_i^A$. This estimate of limb radiance is computed for each limb view for all channels by the Level 1 software, together with an estimate of the random component of uncertainty. The random uncertainty, $\Delta\dot{P}$, on an individual radiance measurement is given by [e.g., *Robinson*, 1974, chap. 20]

$$\Delta\dot{P} \approx \frac{(T_{sys} + T_{sig})}{\sqrt{B\tau}} \quad (14)$$

where T_{sys} and T_{sig} are the radiometer noise and signal brightness temperatures, respectively, B is the predetection noise bandwidth, and τ the postdetection signal integration time. The estimate of random uncertainty associated with each limb radiance calculated by Level 1 software, $\Delta\dot{P}^L$, is dominated by the noise on the individual limb integrations, and includes terms for the random uncertainty on the interpolated space references and gains:

$$\Delta\dot{P}^L = \sqrt{\frac{(T_{sys} + T_{limb})^2}{B\tau} + (\Delta R)^2 + \left(T_{sig} \times \frac{\Delta g}{g}\right)^2} \quad (15)$$

This noise estimate is calculated for all channels each measured limb radiance. ΔR and Δg are the noise on the interpolated space references and channel gains respectively. These are derived from the error covariances in the quadratic fits used for interpolation, where the noise on the individual space and target measurements is given by equation (14).

Measured peak-to-peak gain variations during an orbit are <1% in any channel and are strongly correlated with radiometer temperature variations over an orbital cycle. The noise in interpolated gain is <0.1% rms in the noisiest (narrow) channels and ~0.01% in the quietest (broad) channels. Examples of daily and long-term gain variations in narrow and broad channels of B1 are given in Figure 3 and are representative of performance in the other bands.

MLS views the space reference port every ~16 s (Table 2). Space counts, C_i^S, are interpolated to the times of limb views as described earlier, and the interpolated limb/space count differences are calculated as part of Level 1 processing. This process requires $1/f$ breakpoints of the signal chains to be at frequencies below ~0.01 Hz for the S/N ratio of individual limb measurements not to be significantly degraded by the low-frequency noise on the reference measurements. For MLS the $1/f$ performance is such that the interpolated space counts contribute <1% of the random component of noise in each difference signal for most channels. Figure 4 shows the power spectrum of the noise from channel 2 of B2 obtained by Fourier transforming the time series of space calibration data obtained approximately 2 weeks after

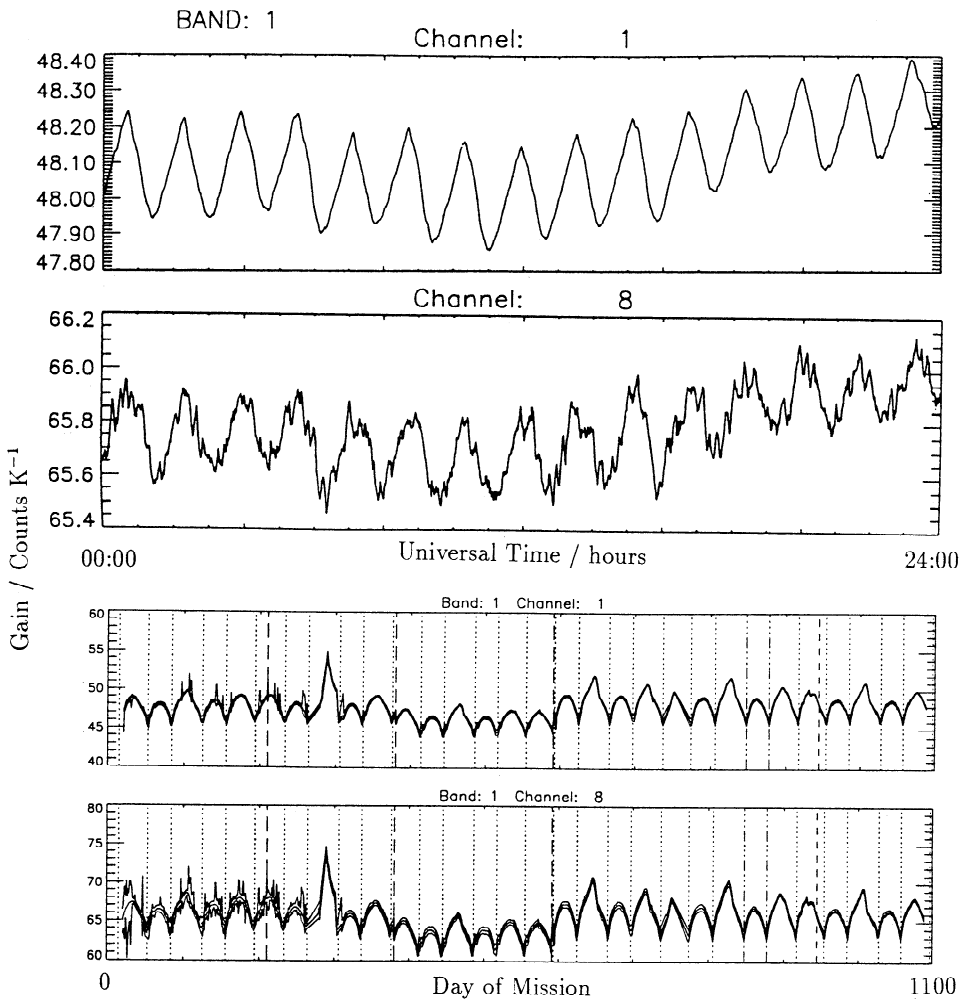

Figure 3. Typical daily (top panels) and long-term (bottom panels) gain variations for channels 1 and 8 of band 1. Ordinates are channel gains in units of counts/Kelvin, computed by Level 1 processing as described in the text. Orbital dependence of channel gains is visible in the top panels, and yaw cycle dependence is evident in the bottom panels (the vertical dotted lines in the bottom two panels indicate when the spacecraft was yawed by 180°, the dashed lines represent significant MLS events, such as change of data integration time). The three lines plotted in the bottom panels are the daily minimum, average and maximum values. The shape and magnitude of gain variations shown is representative of the behavior in all bands.

launch. The random component of uncertainty for individual limb measurements is dominated by the noise on each limb radiance integration, and this noise is Gaussian (as shown by statistical tests on time series of space view data) with correlation times typically longer than ~100 s (C.L. Lau, Characterisation of MLS $1/f$ noise parameters, submitted to *Int. J. Remote Sens*, 1995), allowing the previously described radiometric calibration algorithm to remove any correlation between channels in the low-frequency "noise" due to thermal drifts. Cross-correlation plots of the noise in different channels of a given radiometer indicate that the higher-frequency noise components are uncorrelated.

Digitization of all signals with very low differential nonlinearity is necessary for long-term data averaging to accurately resolve weak signals without contamination by systematic artifacts. Digitized signals may be averaged with confidence only down to levels set by the systematic differences between successive "bits" of the analog-to-digital conversion system. This performance characteristic of the digitizer is called differential, or static, nonlinearity; see, for example, *Hilton* [1993] for further discussion. This is accomplished on MLS by maintaining linear signal chains and by the use of V/F converters for all analog-to-digital conversion.

A strong test of system differential linearity comes from zonal averages of ClO [*Waters et al.*, this issue] for which data are binned over a time period extending up to a month. These data consistently average radiances down to ~0.03 K, a dynamic range of 16 bits. Day–night radiance differences for tangent heights where a negligible signal is expected (above ~65 km) are consistent to ~0.01 K, indicating that system dynamic range extends to at least 18 bits. Level 1 radiances are stored as 16-

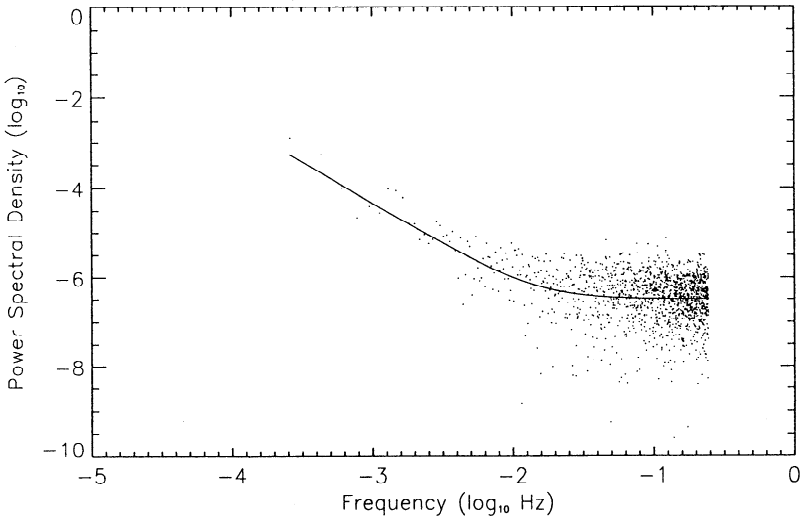

Figure 4. Noise power output spectrum of space port counts from channel 2 of band 2. Solid line is the fitted theoretical curve. Orbital harmonics have been removed. Data for other channels are similar, with breakpoints ranging from 0.06 to 0.002 Hz. These data are taken from *Lau et al.* [1995].

bit integers in units of 0.01 K in order to minimize storage requirements. This representation introduces small systematic artifacts into differenced data sets, preventing averaging down of the noise below 0.01 K. Figure 5 illustrates the ability of MLS to integrate noise down to low levels as determined from prelaunch sensitivity tests in which the instrument was switching between stable targets.

Tasks of the Level 1 processing software also include monitoring individual channel outputs for "spikes" due, for example, to cosmic ray induced upsets and for level shifts due to both commanded and unexpected gain changes. Spikes are defined as deviations in space and target view counts from their values predicted by extrapolation using a quadratic fit which are significantly larger than expected from noise and thermal drift alone; data exhibiting such spikes are marked as "bad." Spikes in limb data are not checked by Level 1 processing, since the radiance variation during a limb scan considerably exceeds the fluctuations due to system noise; potential limb radiance errors are flagged by Level 2 software which routinely computes the goodness of fit between the observed radiance and that from a forward model calculation based on the retrieved constituent profile. Level shifts are handled at Level 1 by marking the data with a "wall" for the affected channel(s) to indicate that estimated gain is discontinuous on either side of this marker and by performing the space count and gain interpolations over valid regions on the appropriate side of the "wall." Spikes and other single event upsets have proven to be very infrequent, typically occurring only once every few weeks; no unexpected gain changes have been observed since launch, except in R3 which failed after ~18 months of in-orbit operation.

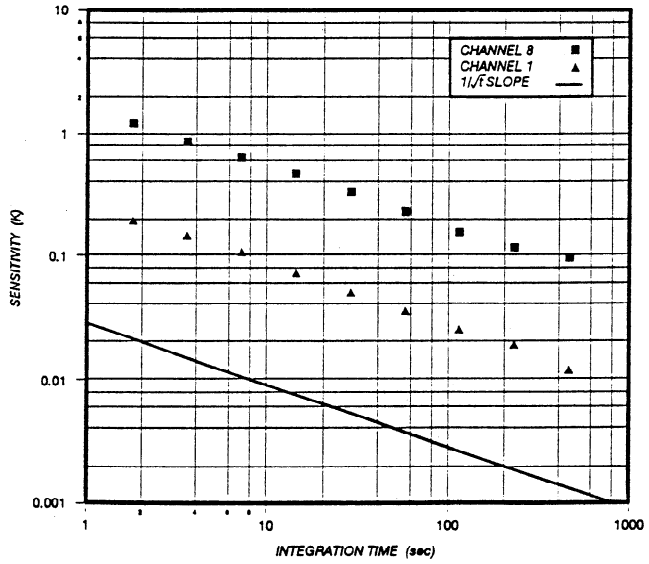

Figure 5. Radiometric sensitivity (Kelvin) versus integration time (seconds) for channel 1 (128-MHz bandwidth) and channel 8 (2-MHz bandwidth) of band 2 obtained from prelaunch tests. The solid line indicates a slope of (integration time)$^{-\frac{1}{2}}$.

Prelaunch Radiometric Calibration

Internal calibration target emissivity and end-to-end system linearity were measured as part of prelaunch radiometric calibration. The FOV-related calibration parameters necessary for the determination of $\dot{P}_i^L$ were also measured, as described in a section below. Target emissivity, 0.9998 or better in all bands, was determined by comparing the reflected power from a silver reference plate to that from the calibration target using Gunn diode oscillators as signal sources. Additional tests were performed to verify that the pyramidal surface structure of the calibration targets did not create diffraction lobes over the frequency range measured by MLS and that there were no significant standing waves

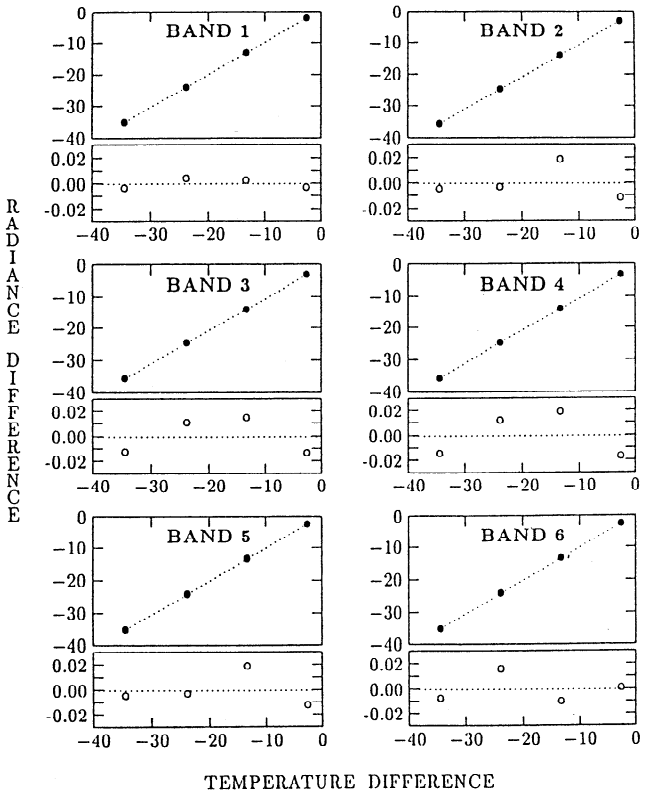

Figure 6. Plots of inferred radiance difference between space and target ports versus temperature difference (Kelvin) of the targets at the two ports, for all MLS bands. Abscissa is temperature difference of the targets on the limb and space ports. Ordinate for larger panels is band-average difference of measured power (Kelvin) from the two targets, and for smaller panels are the residuals (in Kelvin) from the linear fit of input signal-to-instrument response.

in the signal path between the radiometers and the target.

Linearity was measured by switching between the internal ambient calibration target and a similar external target attached to the space port. The external target included heaters to allow its temperature to be precisely controlled and by measuring channel output as a function of the target temperatures, end-to-end system linearity was shown to be better than 0.1%. An example of such linearity test data in all bands is shown in Figure 6.

Independent tests on the filter banks determined their nonlinearity to be less than 0.05% over their full dynamic range. These measurements were performed using a stable noise source as the signal input in conjunction with two precision stepped-attenuators. One of the attenuators was used to step the input signal level through its full range, the other changing the input signal power level by a fixed, relatively small, amount. Linearity was determined by measuring the change in signal counts as the latter attenuator was switched between its two settings at operating points spanning the full input range of each spectrometer. The output power level from the noise source was monitored during the test to allow the effect of drifts to be removed during data processing.

Diagnostics

Internal radiometer noise is measured once per orbit for diagnostic purposes. This is done by lowering the gains of the IF signal chains to their minima, ~40 dB below nominal, for two MMIFs. These data (C_i^Z of Figure 2), combined with the routine measurements of C_i^T and C_i^S, allow determination of instrument noise, $(C_i^O - C_i^Z)$, or T_{sys}, in all channels.

MLS makes its measurements in a "total power" mode in which several atmospheric signal integrations are performed without any intervening reference measurements. This method of measurement is especially sensitive to gain and offset changes, the dominant sources of variability over the 11 MMAF calibration processing window arising from thermal variations and $1/f$ noise. Level 1 software interpolates space counts onto the times of all MMIFs in each MMAF as discussed previously. Differences between interpolated and measured space counts at the times of the space measurements are used for determination of the χ^2 statistic, and this quantity is calculated and examined as part of MLS daily health and performance monitoring. Figure 7 gives a typical daily time series of band average χ^2 for all MLS bands, and Figure 8 shows the corresponding daily average χ^2 for each channel. Figure 7 shows that B1 through B4 exhibit uniform performance in contrast to B5 and B6. B6 is affected by noise from the Gunn diode local oscillator, discussed below under channel shape calibration. The plots in Figure 8 indicate that while the narrower center channels of the spectrometers are dominated by white noise ($\chi^2 \approx 1$), there is a noticeable contribution to interpolated space count error from low-frequency noise over the timescales of minutes in the inherently more sensitive broader outer spectrometer channels.

Use of in-Orbit Data for Radiometric Calibration

Part of the calibration philosophy for MLS was that prelaunch calibrations be sufficiently comprehensive and accurate to allow all major measurement objectives to be met using these data, with validation and possible minor refinement from in-orbit data. MLS uses the days on which the spacecraft performs the periodic yaw maneuver for occasional onboard software updates, to perform special operations to monitor instrument characteristics in more detail than provided by data from routine operation and also to provide data for calibration refinement.

Temperature gradients in the internal calibration target were anticipated from the results of ground tests. These were characterized early in the mission with tests which exposed the surface of the target to space via the limb port for varying lengths of time and then observing target radiance for several MMIFs with the cooling path to space blocked by the switching mirror. A skin

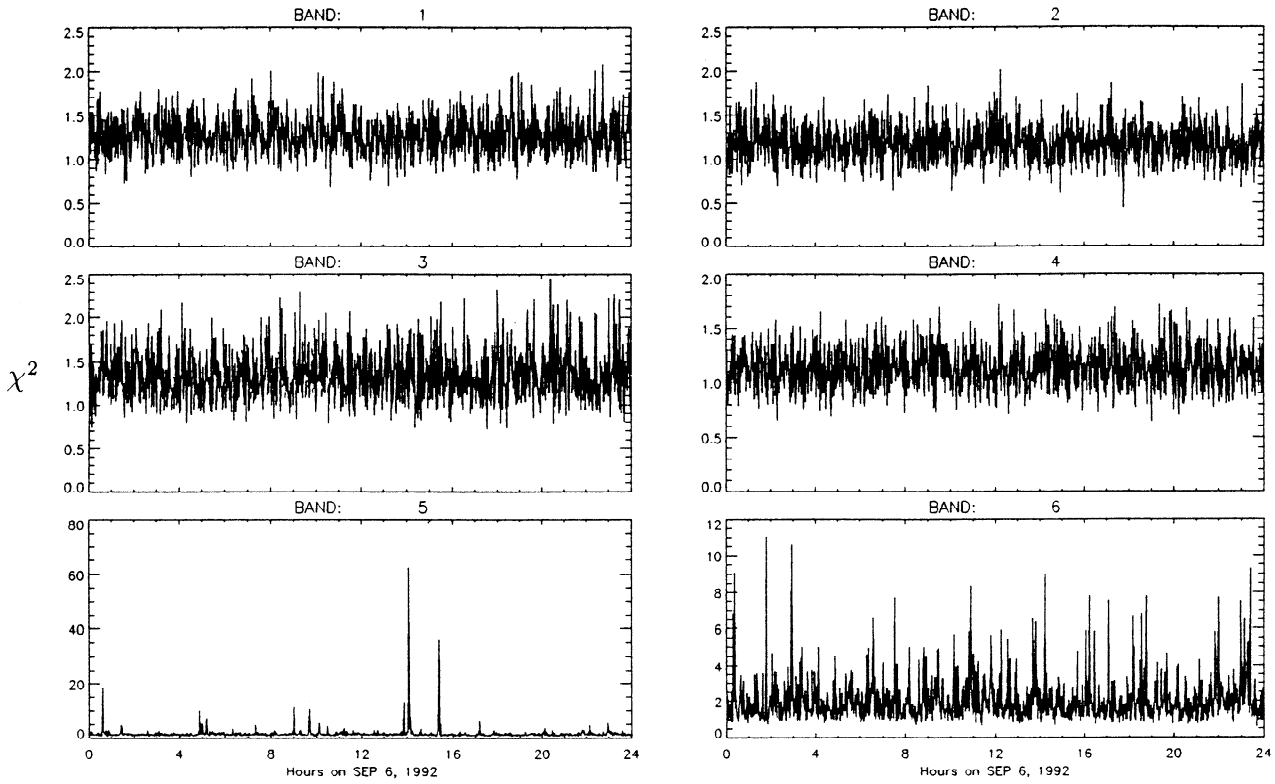

Figure 7. Typical daily time series band-average space-view χ^2 plots for all MLS bands. A value of unity indicates spectrally flat noise at the level predicted from measured system temperatures. The sporadic interference in B5 and elevated overall χ^2 in B6 (compared to B1–4), are typical for these bands.

depth (and hence band) dependent relaxation of target radiance was observed as the target material regained thermal equilibrium, but its amplitude is at such a low level (<0.5 K) as to impart negligible error in radiometric gain calibration.

Additional tests have measured the slew rates of the antenna and switching mirror mechanisms to monitor potential degradation and the $1/f$ characteristics of all signal channels. After 2.3 years in orbit (in late December 1993), MLS began to exhibit signs of wear in the antenna-scanning mechanism, manifesting as occasional "slips" during the limb scan. Antenna scanning was subsequently changed from open to closed-loop control via changes in the onboard software, so that slips are detected and corrected as soon as they occur, and both onboard and ground software has been modified to monitor scan mechanism performance more closely. Scan slips became much more severe in late 1994, and the scan pattern, together with other details of instrument operation, were changed to prolong instrument lifetime. Since these changes were implemented, no additional scan slips have occurred to date (February 1996).

Radiometric Calibration Summary

Systematic errors and uncertainties in radiometric calibration arise from errors and uncertainties in knowledge of (1) calibration target emissivity; (2) calibration target temperature, including temperature gradients; (3) switching mirror baffle transmissions and emissions; and (4) antenna ohmic, diffraction and scattering losses; and from (5) system nonlinearity.

Systematic effects manifest as both scaling (multiplicative) and offset (additive) uncertainties and errors in calibrated radiances. The random component of uncertainty in each calibrated limb radiance arises from radiometric noise on limb and calibration data integrations and can be reduced by data averaging. Table 3 summarizes scaling and random uncertainties from the sources discussed above for all MLS bands. The scaling uncertainties are dominated by FOV-related contributions, described below. Two random uncertainties are given for each band, the first (smaller) number corresponding to the noise in a single ~1.7-s limb integration for a broad (128 MHz) channel, the second for a narrow (2 MHz) channel, and each includes the effects of noise on calibration (space and target) views. Radiance offset uncertainties, currently handled by Level 2 processing, are not listed here. The radiance offsets vary smoothly (by ~1 K in all bands) during a spacecraft yaw period (~36 days).

Spectral Calibration

Spectral calibration is the determination of the end-to-end frequency response, $F_i(\nu)$, of each channel. There are two primary contributors:

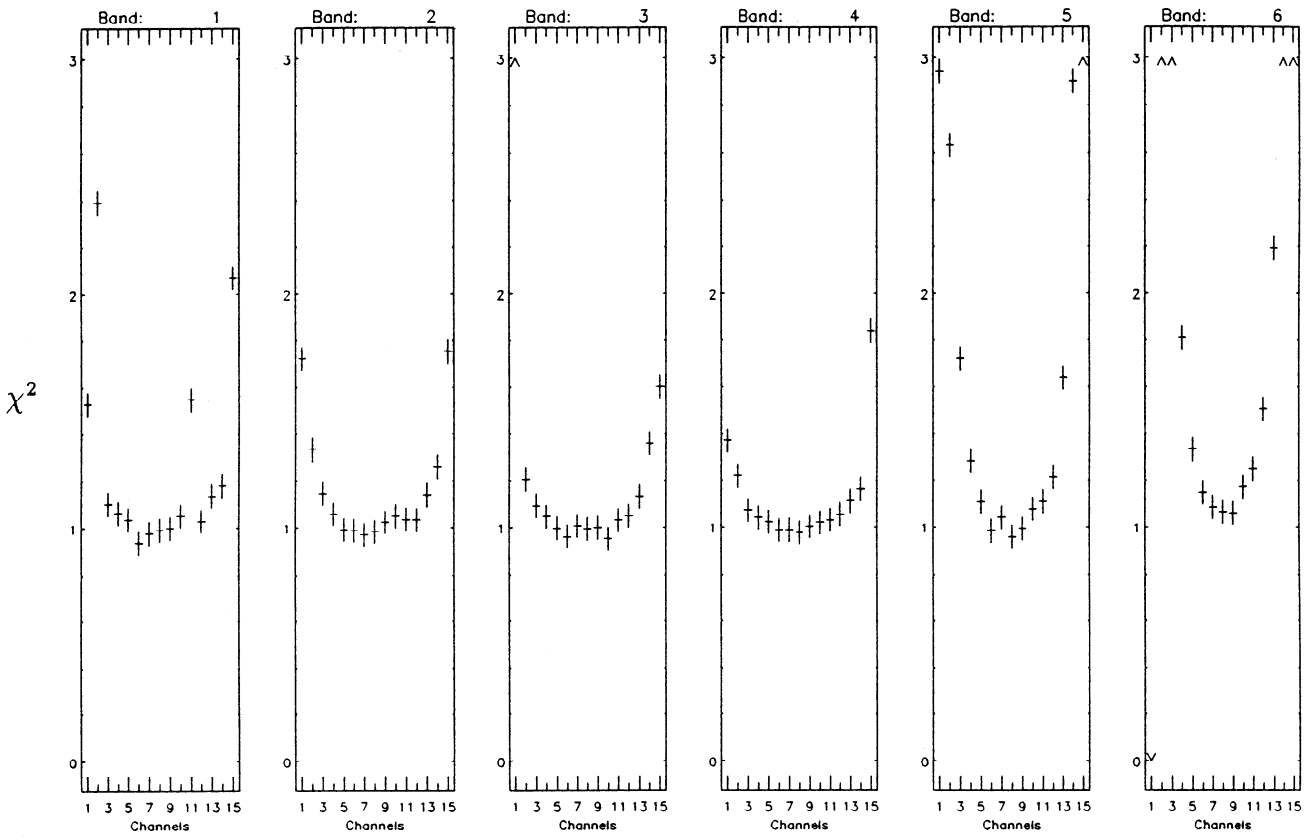

Figure 8. Typical daily-average space-view χ^2 for all MLS channels. The center channels of all bands exhibit the theoretically expected noise levels ($\chi^2 \approx 1$), with contributions from nonspectrally flat noise components in the more sensitive wing channels. Channels 2 and 11 of B1 exhibit elevated χ^2 because of interference from internal MLS local oscillator signals.

1. The detailed spectral response of each channel (the "channel shape") is dominated by the individual spectrometer channel filter elements, with significant influence from electronic elements earlier in the signal chains for some of the broader ($\geq$32 MHz wide) channels.

2.The two major responses in the radiometer upper and lower sidebands, symmetrically dispositioned on either side of the first local oscillator (LO) frequency but with slightly different responses.

For bands in which the atmospheric signals appear primarily in a single sideband (all except B1), it is referred to as the signal sideband; the other response is referred to as the image sideband.

Table 3. Summary of Radiometric Calibration Uncertainties

Band	Scaling, %	Random, K
1	2.6	0.03 – 0.21
2	1.6	0.07 – 0.51
3	1.6	0.07 – 0.53
4	1.6	0.10 – 0.79
5	1.7	0.13 – 0.90
6	1.7	0.14 – 1.00

Scaling uncertainties (estimated 3σ values are given here) arise mostly from FOV-related uncertainties (the first row of Table 8). Random uncertainty is the double sideband rms (1σ) noise on an individual ~1.7-s measurement of limb radiance, including the effects of $1/f$ noise and noise on calibration measurements; the range given for each band encompasses broad (128 MHz) and narrow (2 MHz) channels. It should be noted that the noise levels given by *Barath et al.* [1993] are single sideband values (approximately twice the values given here.)

Channel Shape

The calibrated signal power inferred for each channel, $\dot{P}_i$, is an average of the product of the signal power spectral density, $P(\nu)$, and end-to-end frequency response of the channel, $F_i(\nu)$:

$$\dot{P}_i = \frac{\int P(\nu) F_i(\nu) d\nu}{\int F_i(\nu) d\nu} \tag{16}$$

where the integrals are evaluated over the full range of frequencies for which there is significant instrument response, and angular dependence of instrument response and input signals over this range has been ignored. MLS spectrometers use conventional inductor-capacitor (LC) filters in the outer (32- to 128-MHz width) channels and surface acoustic wave (SAW) filters in the narrower center (2- to 16-MHz width) channels. The SAW filters have numerous ripples in their passbands, and all channels can have appreciable atmospheric radiance variation across their width, requiring $F_i(\nu)$ to be character-

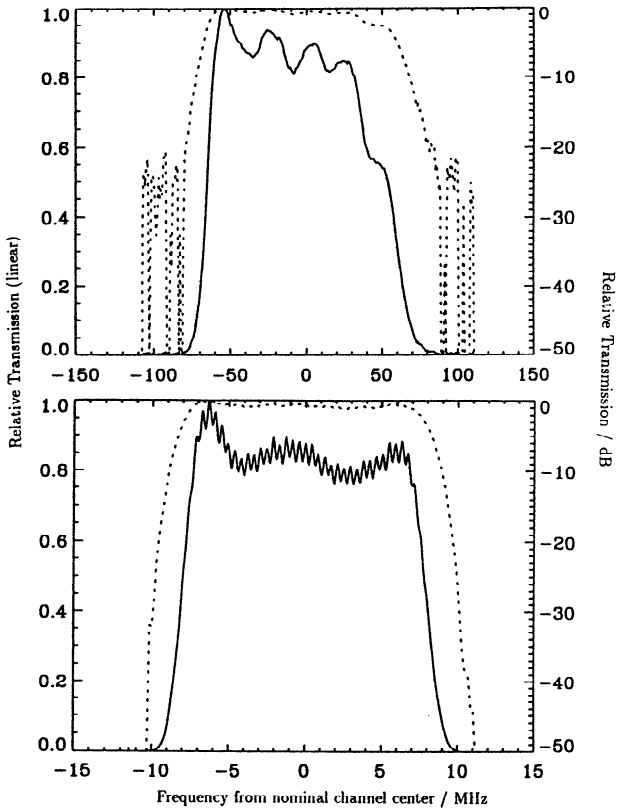

Figure 9. Measured LC (top) and surface acoustic wave filter channel responses. Frequencies on the abscissa are megahertz from nominal channel center. Left-hand ordinate axis is normalized linear transmission (solid curves), right hand axis is for logarithmic response (dashed curves). Top plot is for B1, channel 1; bottom plot is for B1, channel 4.

ized by several tens to hundreds of spectral points in each channel.

End-to-end sweeps using a synthesized source referenced to a cesium frequency standard allowed direct measurement of $F_i(\nu)$ in the broad outer channels of all bands in both sidebands of all radiometers. The source output was coupled into the radiometers optically via an external parabolic mirror on the space port. All source and instrument operation, monitoring, and data acquisition were controlled by the Ground Support Equipment (GSE) computer. Source output power was monitored during sweeps using power meters built into the source output waveguides. The measurement sequence for the filter sweeps included regular periodic calibrations using the internal switching mirror, which allowed channel gain and offset drifts to be continuously monitored, and compensated for, in data processing. Tests on the Vibration Test Model (VTM) of MLS indicated that end to end and spectrometer level sweeps of the narrower($\leq$16 MHz) channels produced consistent results, and for the flight model MLS only the 32 MHz and broader channels were characterized end to end. Figure 9 shows examples of LC and SAW filter channel responses measured through the entire MLS signal path. The shapes from prelaunch calibrations are for the sidebands containing the largest atmospheric signal radiances, the upper sideband for B1 to B4, and the lower sideband for B5 and B6.

The synthesized source was also used to perform a broad (178 to 210 GHz) end-to-end sweep with moderate resolution (~4 MHz) to verify that the downconversion processes prior to the spectrometers had not introduced any unexpected spurious responses in B2 to B6.

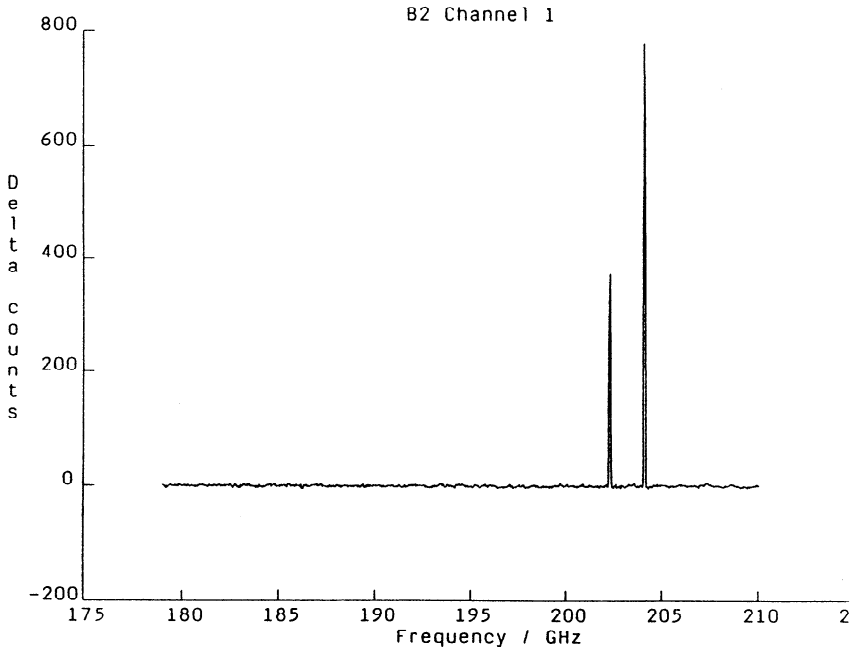

Figure 10. Output counts from the V/F converter of B2, channel 1 measured during an end-to-end sweep over the range 178 to 210 GHz. The two sideband responses about the first LO are clearly visible, with most of the apparent difference in response arising from variations in transmitter output power.

The dynamic range of the measurements ranged from ~20 dB to ~32 dB, depending on transmitter power output and channel width and gain. Figure 10 shows a typical output signal obtained during this test.

Uncertainties in calibrated radiance arising from the estimated uncertainties in channel shape were determined by numerical modeling using equation (16). Radiance profiles similar to expected atmospheric signals were combined with measured and perturbed channel shapes to determine the error in calculated $\dot{P}_i$ corresponding to the estimated uncertainties in $F_i(\nu)$. The resulting worst-case uncertainties in calibrated radiance were less than ~0.25% in B1 to B4, ~0.5% in B5 and B6, and 1% in the outermost channels of B6. Bands B5 and B6 have larger uncertainties than the others because of the poorer S/N of the calibration measurements. Input to the filter bank for B6 is attained via a single downconversion, and its lowest intermediate frequency (IF) channels are affected by noise from the relatively nearby LO. This noise arises from the Gunn diode and possibly also from vibrations in the grids of the Fabry-Pérot interferometer (FPI) diplexer used to combine the first LO and signal beams. Since the edge of the first IF passband for B6 is within ~200 MHz of the first LO frequency, FPI grid vibrations (due to switching mirror movement) modulate the signal path transmission, imparting additional noise to the measured signals. This additional noise appears only for a very narrow range of spacecraft power bus voltages which cause the switching mirror motor step rate to excite a mechanical resonance associated with the FPI. This phenomenon did not arise until the spacecraft end-of-night bus voltage had decreased due to battery aging (after 1 year of in-flight operation) and is handled by inhibiting switching mirror operation for two periods per orbit (totaling ~3 min) when the bus voltage is in the problem range. This reduction in calibration views has negligible effect on data quality.

The scaling error depends upon the shape of the radiance profile being analyzed by a filter channel, being zero when the radiance is constant across the channel passband (e.g., as when viewing a saturated signal or space), and worst-case systematic scaling errors arise when the change in radiance across a channel passband is a maximum.

Sideband Response Calibration

Relative sideband responses of the radiometers were measured using an external scanning FPI as a tunable filter while switching between views to external calibra-

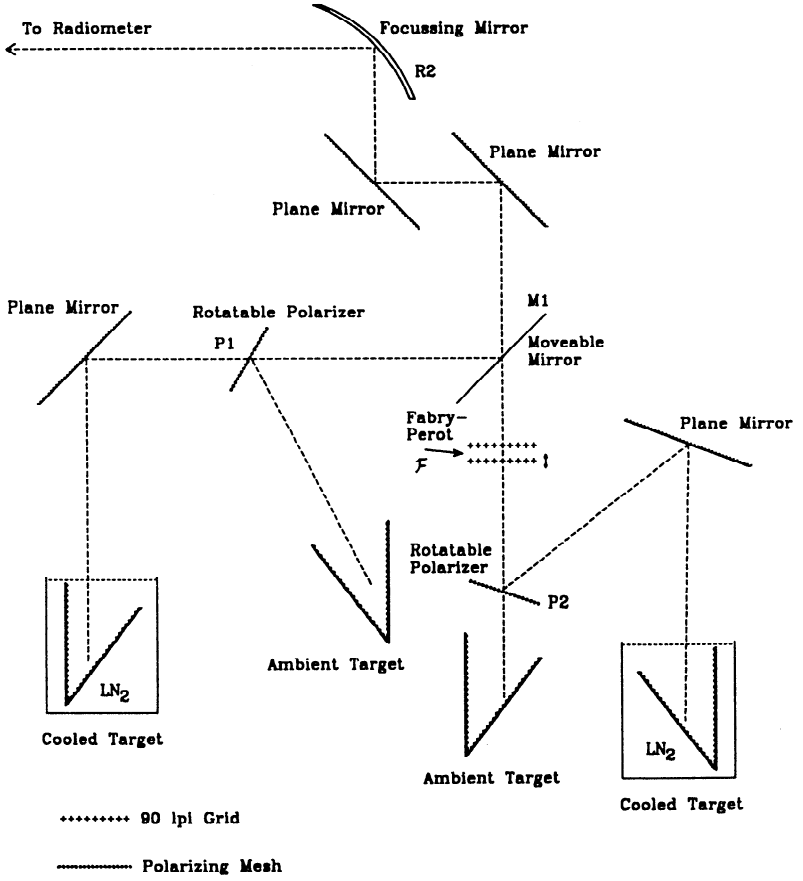

Figure 11. Layout of apparatus used to measure relative sideband response of B2 through B6. The scanning Fabry-Pérot interferometer ($\mathcal{F}$) implements a tunable bandpass filter. M1 directs the instrument FOV to a calibration path and moves out of the beam to enable the path through $\mathcal{F}$. Both paths contain ambient and liquid nitrogen (LN_2) cooled targets, separately selected via rotating polarizers.

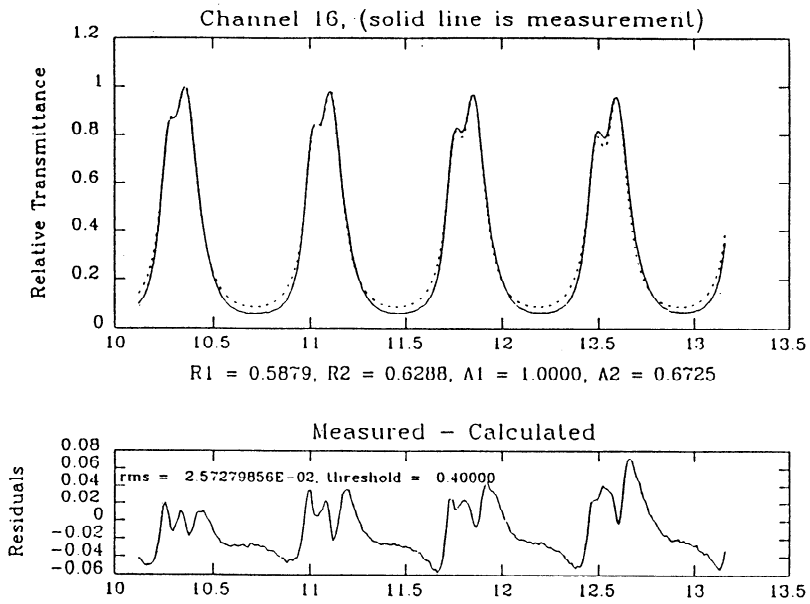

Figure 12. An example of MLS sideband sweep data (top panel) for a 128 MHz-wide channel in B2. Dashed line is calculated response, after fitting to the measurements. Vertical axis of the top panel is relative transmission (linear scale), horizontal axis is FPI grid separation in millimeters. All channels were swept through 4 orders of the FPI. Relative sideband response was determined from least squares fits of calculated and measured responses in individual transmission orders to reduce errors from unmodeled walk-off in the FPI (see text). Bottom panel shows difference between measured and fitted (calculated) FPI transmissions.

tion targets at ambient and liquid nitrogen temperatures, as shown in Figure 11. A similar pair of targets, viewed via a path bypassing the FPI, provided periodic gain calibration. The GSE computer controlling MLS also operated the mechanisms for switching between views of the four external targets and for varying the FPI grid spacing. Grid spacing was stepped over the ranges 10 to 13 mm, and 30 to 33 mm, in steps of 0.01 mm to allow all channels in bands B2–B6 to be swept through at least 4 orders of the FPI. Results from the sweep of a 128-MHz-wide channel in B2 are shown in Figure 12. Figure 13 shows measured relative sideband response in B1 (top panel), B2 through B4 (middle panel) and B5. The *N*-shaped line in the top panel is the manufacturer's sideband data, and the horizontal line segments are the positions and widths of the MLS channels in B1, with vertical segments at the sideband responses used in ground processing. The solid lines in the bottom panels are the quadratic fit to the FPI data used in ground processing for bands B2 to B6. For B6 the prelaunch sideband calibration data were considered unreliable because of measurement limitations imposed by the narrow frequency separation between the signal and the image sidebands, and the fit to the measurements for this radiometer was constrained to unity sideband ratio at the radiometer center frequency, in accordance with results from prelaunch modeling (B. Maddison, private communication, 1991) of 183 GHz mixer performance.

Even though the FPI was swept through at least 4 orders in bands 2 to 6, it can be seen from Figure 12 that the peak relative transmission of each order decreases as grid separation increases. This is mainly due to "walk-off," the increase in size of the beam as it performs multiple reflections between the FPI grids. This occurs because the product of the FPI finesse and grid spacing is greater than the Rayleigh distance of the signal beam (that is, the beam relecting between the FPI grids is not sufficiently close to planc-parallel). Walk-off was not modeled in the software which performed the least squares fits between measured and modeled transmissions, and so sideband ratio was determined from individual fits to each of the FPI transmission orders, not to all orders simultaneously.

Because the atmospheric emission signals in both sidebands of B1 are similar in magnitude, retrieved tangent pressure is relatively insensitive to errors in sideband calibration. Recent studies of B1 residuals indicate that significant errors (up to a factor of ~2 at one band edge) are likely in the sideband data for B1 given in Figure 13, resulting in worst-case tangent altitude errors of ~200 m, and a correspondingly small error in temperature, for MLS Version 3 data. More accurate sideband ratios for B1 are currently being determined from atmospheric data by minimization of radiance residuals. Examination of these preliminary sideband data indicates that the major features, such as ratios of sideband response in adjacent channels, are consistent with data (not included on Figure 13) obtained from the prelaunch spectral calibration synthesizer sweeps.

The rms differences between measured and calculated FPI transmissions above a selected transmission threshold are used as the estimate of relative sideband re-

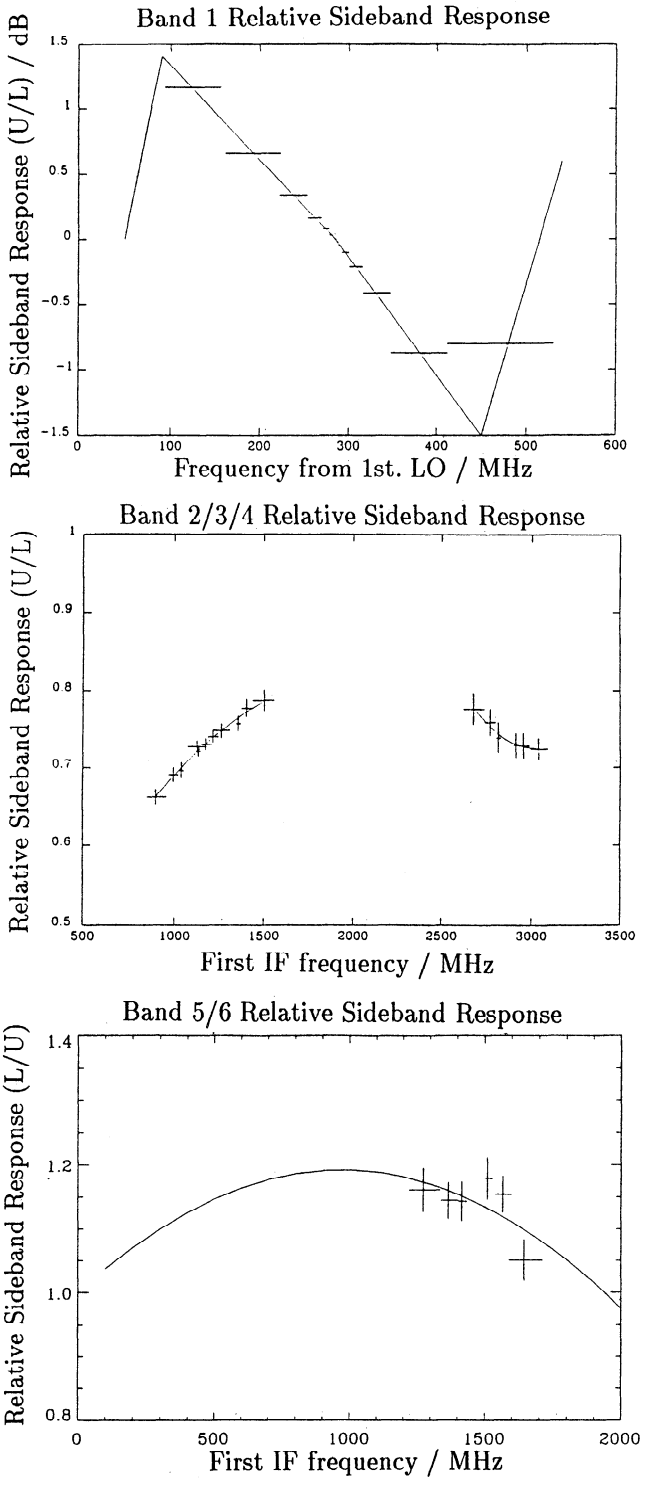

Figure 13. MLS relative sideband response in B1 (top panel), B2 through 4 (middle) and B5 and B6 (bottom). The N-shaped curve in the top panel is the manufacturer's sideband response data, and the horizontal line segments are at the positions of the MLS filter channels for B1, at the relative responses used in data processing. For the bottom two panels the crosses are measurements; horizontal extents are measured channel widths, vertical extents are rms differences between measured and fitted FPI transmissions, and the curves are fits used in data processing. Bottom panel shows measured responses for only B5; see text for additional comments on B6.

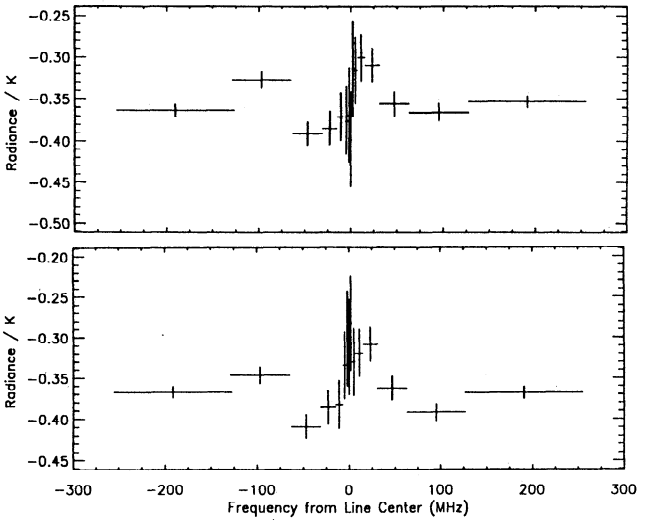

Figure 14. Typical spectral baseline for B2 (top panel) and B3 (bottom). These spectra are the average of calibrated limb radiances for views with tangent heights above ~90 km in the latitude range 20°N to 50°N for 1 day's data (~10 min integration time) generated by Level 1 processing. The spectrally varying component is stable to ~0.05 K, but the average offset drifts by ~5 K in all bands throughout a spacecraft yaw cycle (~36 days).

sponse uncertainty by the fitting software. The channel dependent transmission threshold is typically 0.4, rising to 0.5 in some channels of bands B4 to B6, to avoid biases from fitting to the regions of low transmissions which provide least information on relative sideband response but include the largest systematic artifacts. These rms differences correspond to uncertainties in calibrated radiance of ~0.6–1% in bands B2 to B4 and ~2% in B5. For the purposes of error estimation during data validation, an rms uncertainty of 7% is estimated for B6.

The FPI approach to sideband response calibration was chosen in preference to one using a calibrated narrowband swept source (such as the channel shape sweeper) for several reasons; many channels could be calibrated simultaneously, and limitations imposed by standing waves between source and instrument, and within the measurement apparatus itself (particularly in the path to the power level monitors) are much easier to overcome.

Spectral Baseline

The views to space from the switching mirror via the antenna and space ports are truncated slightly differently since the optical paths are different, and the approximately Gaussian MLS optical beam shapes do not drop off completely to zero at baffle and mirror boundaries. Since beam shapes are necessarily frequency dependent in a coherent system, the different truncations give rise to a small frequency dependent signature (spectral baseline) in addition to a larger frequency independent offset from antenna scattering losses and emis-

sion, when viewing to space via the two paths. Since MLS uses the signal from the space port as the reference against which the limb signals are differenced, it is necessary for this baseline to be small, stable, and scan independent.

The spectral component of the baseline is removed during Level 1 processing by subtracting a channel dependent offset determined from daily averages of radiances measured at tangent heights where there is negligible atmospheric signal. Figure 14 shows typical spectra for atmospheric views with ~90-km tangent height in bands B2 and B3 (the bands where spectral baseline is most important because of the relatively weak ClO signal). A 10° roll maneuver of the spacecraft allowed MLS to verify the scan independence of this baseline by performing antenna scans while viewing high above the Earth's limb where there is no atmospheric spectral contribution. Long-term data analysis for trends indicates that this correction is stable to ~0.05 K.

Use of in-Orbit Data for Spectral Calibration Validation

The positions and stabilities of individual channel centers can be confirmed by the study of radiance residuals which are very sensitive to these parameters [*Froidevaux et al.*, this issue]; there is no detectable error in prelaunch spectral calibrations except for sideband data for B1 and B6, confirming the long-term stabilities of both the individual channel filters and the common master oscillator frequency reference.

Spectral Calibration Summary

The uncertainties in calibrated radiance arising from uncertainties in channel shape and relative sideband response are summarized in Table 4. Both channel shape and relative sideband uncertainties translate into radiance scaling errors with no offset or significant time-varying random components.

Scaling uncertainties arising from uncertainty in channel shape depend upon the form of $P(\nu)$, being negligible when there is a small variation in $P(\nu)$, and a maximum when $P(\nu)$ has greatest change across a channel passband. The values given in Table 4 are 3σ estimates for worst-case atmospheric radiance profiles.

The relative sideband uncertainties in Table 4 are the rms differences between measured and calculated FPI transmissions, described earlier, converted into equivalent single sideband radiance errors. For B1, no sideband sweeps were performed, and manufacturer's data for sideband response of the 63-GHz mixer is given. These data are now believed to contain errors which introduce worst-case errors in retrieved tangent pressure equivalent to ~200 m at the limb (and a correspondingly small error in temperature). For B6, similar difficulties with degraded S/N were noted during sideband calibration as discussed above under channel shape calibration. Additionally, for the channels closest to the first LO in B6, the narrow frequency separation of signal and image responses did not allow good relative sideband response measurements across the entire band. As a result, the decision was made to use the sideband responses predicted from Figure 13 for data processing and to update these responses based on in-flight comparisons of the O_3 profiles measured in bands B4 and B6.

Table 4. Summary of Estimated Uncertainties in Calibrated Limb Radiance Arising From Uncertainties in Channel Shape and Relative Sideband Response

Band	Channel Shape Uncertainty, %	Relative Sideband Uncertainty, %
1	0.25	see text
2	0.25	0.6
3	0.25	0.7
4	0.25	1
5	0.5	2
6	0.5 – 1	see text

Scaling uncertainties arising from channel shape uncertainty depend upon the radiance profile being analyzed, and the values given are 3σ estimates for worst-case atmospheric radiance profiles. Relative sideband uncertainties are scaling errors in single sideband radiance and are the rms (1σ) differences between measured and calculated Fabry-Pérot interferometer sweep signals.

Field-of-View Calibration

FOV calibration consists of the determination of the relative response of the MLS, as a function of direction and polarization, to received power. Optical path losses in front of the switching mirror are also included, since they too appear in equation (8). Table 5 summarizes the antenna FOV performance measured before launch. Dependences of the FOV on scan position, orbital conditions, and signal frequency within bands, all small compared to its angular dependence, were also characterized, allowing their contributions to tangent pressure and ozone uncertainties to be evaluated during data validation [*Fishbein et al.*, this issue, *Froidevaux et al.*, this issue].

For calibration the 4π solid angle domain of the FOV is divided into two parts, conforming to the first two levels of MLS data processing. Inside Ω_A, the solid angle extending ± 0.1 radian about the nominal boresight direction, $G_r^A(\theta, \phi)$ is used in equation (8) by the forward model to produce coefficients used in Level 2 processing. Integrating far sidelobes over the remaining $4\pi - \Omega_A$ provides η_r^A for equation (9), which is used in Level 1 processing. Further differences in the characterization of FOV at the two levels are as follows:

1. The FOV response outside Ω_A is $< 10^{-5}$ of its peak value. However, the antenna's on-axis gain is so large (ranging from 4.3×10^5 for R1 to 3.4×10^6 for R2) that the average FOV response outside Ω_A must be characterized to 10^{-8}. As this was only possible for B1, given the available test equipment and far-field range, certain calibration data depend on analytical models. Since the radiance outside Ω_A is relatively constant and/or difficult to model (e.g., Earth, MLS/UARS structures,

Table 5. MLS Antenna FOV Performance From Prelaunch Calibration and Analytical Models

Parameter	R1 (B1) 63 GHz	R2 (B2–4) 205 GHz	R3 (B5–6) 183 GHz
Half-power beam width (HPBW) (vertical), deg	0.206	0.064	0.077
uncertainty	0.006	0.003	0.003
HPBW (horizontal), deg	0.43	0.145	0.152
uncertainty	0.023	0.008	0.006
Beam efficiency	0.91	0.90	0.91
uncertainty	0.01	0.01	0.01
Polarization (angle between **E** and vertical at 30-km tangent point), deg	114.	91.	2.
Peak cross-polarization, dB	−30	−19	−20
FOV direction (dFOV) uncertainty (vertical), deg :			
absolute, B1 to optical reference cube	0.0036		
relative to B1		0.0016	0.0021
Transmission ρ_r^A (ohmic efficiency)	0.992	0.989	0.99
Transmission η_r^A (wide-angle efficiency due to scattering, edge diffraction, and primary spillover)	0.931	0.976	0.921

All uncertainties are 3σ. Beam efficiency is defined as the fraction of power the MLS would receive from within a cone of half-angle 1.25 × HPBW, centered at the FOV direction, if it were enclosed in an isotropic radiation field. It describes the diffraction efficiency of the antenna pattern's main lobe in the same way η_r^A describes that of the FOV within Ω_A.

and space), calibration data used in Level 1 processing are constant FOV transmissions and radiance offsets. These are η_r^A, ρ_r^A and $\dot{P}_r^{OA}$, $\dot{P}_r^{SA}$ in (9), and η_r^{MX}, $\dot{P}_r^{BX}$ in (6), with $X = L$, S and T. The factor $(1-\eta_r^A)$ in equation (9) characterizes the instrument's susceptibility to stray radiance within the finite apertures of the antenna. We refer to such effects as spillover, by analogy with transmitting antennas.

2. Both the atmospheric signal and the FOV vary rapidly with angle inside Ω_A. Here, detailed FOV response is needed by the forward model (*W.G. Read et al.*, manuscript in preparation, 1996).

Level 1 FOV Parameters

Level 1 FOV calibration parameters are the transmissions ρ_r^A and η_r^A and associated effective brightnesses $\dot{P}_r^{OA}$ and $\dot{P}_r^{SA}$, averaged over the antenna reflectors. To calculate them, we derive a more detailed form of equation (9), identifying the dependence on each reflector and its geometry. First, we project all apertures to the radiometer limb port plane, dividing it into regions. The power incident on each region originates from a solid angle having a characteristic brightness and reaches this plane through some combination of the MLS reflectors. Then the radiance incident on the limb port is given, for channel i in radiometer r, by

$$\begin{aligned}\dot{P}_i^A = {} & \rho_r^1\rho_r^2\rho_r^3\eta_r^{AA}\eta_r^1\dot{P}_i^L \\ & + \rho_r^1\rho_r^2\rho_r^3(1-\eta_r^{AA})\eta_r^1\dot{P}_r^{SL} \\ & + (1-\rho_r^1)\rho_r^2\rho_r^3\eta_r^1\dot{P}_r^{O1} \\ & + \rho_r^2\rho_r^3(\eta_r^2-\eta_r^1)\dot{P}_r^{S1} + (1-\rho_r^2)\rho_r^3\eta_r^2\dot{P}_r^{O2} \\ & + \rho_r^3(\eta_r^3-\eta_r^2)\dot{P}_r^{S2} + (1-\rho_r^3)\eta_r^3\dot{P}_r^{O3} \\ & + (1-\eta_r^3)\dot{P}_r^{S3} \end{aligned} \quad (17)$$

where

ρ_r^k = reflectivity of reflector $k = 1, 2, 3$ (primary, secondary, tertiary);

η_r^{AA} optical transmission of the antenna system: the product of scattering (η_r^{AS}) and diffraction (η_r^{AD}) from the primary aperture plane;

η_r^k optical transmission of reflector k for radiometer r;

$\dot{P}_i^L$ limb radiance power, channel i;

$\dot{P}_r^{SL}$ radiance power in the limb hemisphere but outside the FOV measurement angle Ω_A;

$\dot{P}_r^{Sk}$ radiance power illuminating the spillover solid angle for reflector k;

$\dot{P}_r^{Ok}$ power thermally emitted by reflector k.

Values of ρ_r^k, η_r^k and η_r^{AA} ($= \eta_r^{AS}\eta_r^{AD}$) account for four loss mechanisms contributing to antenna transmission and radiance.

Reflectivities ρ_r^k of the antenna reflectors. These were inferred from reflectivity measurements in all bands, using a silver plate standard whose reflectivity was calculated from the Fresnel formulas [*Born and Wolf,* 1980] with DC conductivity $\sigma = 6.14 \times 10^7$ mho/m. For example, the smallest reflectivity measured was 0.9968 with a standard deviation of 0.0008, for the primary reflector at 205 GHz. Multiplying this by the calculated silver plate reflectivity, 0.9988, we infer an absolute reflectivity of 0.9956 in B2–4. Antenna transmission ρ_r^A (ohmic efficiency for radiometer r) in Table 5 is a product of inferred reflectivities of all three antenna reflectors. Combining measurement and systematic errors, we estimate total 3σ uncertainties in ρ_r^A to be 0.003 for B1 and 0.004 for B2–B6.

Optical transmissions η_r^k at each antenna reflector. These were obtained by integrating feed patterns (wide-angle FOVs measured for each radiometer subassembly) to the projected outlines of the reflectors. Similar integrations to the limb, target and space port edges gave the baffle transmissions η_r^{MX} in equations (5) and (6).

Scattering η_r^{AS} by antenna surface irregularities. This was estimated using the contour measurements made during the manufacture of the reflectors, on both coarse (two dimensional) and fine (one dimensional) grids. The two-dimensional data set was used to calculate errors of reflector figure (such as tilt, defocus and astigmatism), for antenna alignment. Fourier analysis of the one-dimensional data set yielded rms surface deviation and an associated correlation length [*Marx et al.,* 1990]. These were used with the Ruze statistical model [*Ruze,* 1966], to estimate the scattered power which is too small to be seen in the measured FOV patterns. The estimated loss due to scattering is budgeted in the antenna transmission term. Mean values of the first three or four sidelobes measured for B2–B4 matched the predicted scattered pattern envelope. Model errors of 10% in rms surface deviation and 15% in the associated correlation length give 40% uncertainty in fractional scattered power $1 - \eta_r^{AS}$, corresponding to 0.7 K in radiance offset for the worst case (B5 and B6).

Edge diffraction η_r^{AD}. A model was developed by applying the geometrical theory of diffraction (GTD) to the primary reflector leading edge (the limiting aperture at -15 dB taper). Applying the aperture-field method to measured feed patterns gave a power level adjustment for patterns predicted by the GTD. These were then validated by comparison with sidelobes measured near 6° from boresight of the B1 FOV, for which spillover is greatest and edge diffraction is most pronounced; η_r^{AD} ranges from 0.977 ± 0.009 in B1 to 0.998 ± 0.001 in B2–B4.

For simplifying equation (17) to equation (9) the net ohmic transmission $\rho_r^A = \rho_r^1\rho_r^2\rho_r^3$ is the product of measured component reflectivities. Similarly, the antenna transmission $\eta_r^A = \eta_r^{AA}\eta_r^1$ depends on scattering, diffraction, and primary reflector spillover losses. To derive an effective radiance $\dot{P}_r^{OA}$ from the radiances and temperatures in (17), we assume the antenna is isothermal and match terms, giving

$$(1-\rho_r^A)\dot{P}_r^{OA} = \left[(1-\rho_r^1)\rho_r^2\rho_r^3\eta_r^1 + (1-\rho_r^2)\rho_r^3\eta_r^2 + (1-\rho_r^3)\eta_r^3\right]\dot{P}_r^{Ok} \tag{18}$$

which we solve for $\dot{P}_r^{OA}$ using an average of $\dot{P}_r^{Ok}$ over all orbital conditions.

Likewise, knowing the antenna geometry, we estimate stray radiances $\dot{P}_r^{Sk}$ in (17) by $\dot{P}_r^U$ for UARS/MLS structure and $\dot{P}_r^H$ for the forward hemisphere, giving for $\dot{P}_r^{SA}$:

$$\dot{P}_r^{SA} = \left\{\dot{P}_r^U[\rho_r^2\rho_r^3(\eta_r^2 - \eta_r^1) + (1-\eta_r^3)] + \dot{P}_r^H[\rho_r^1\rho_r^2\rho_r^3(1-\eta_r^{AD})\eta_r^1 + \rho_r^3(\eta_r^3 - \eta_r^2)]\right\}/[(1-\eta^A)\rho_r^A]. \tag{19}$$

For prelaunch calibration (Table 5), ρ_r^k and η_r^k were measured, η_r^{AD} was modeled, and $\dot{P}_r^{SL}$, $\dot{P}_r^{Sk}$, and $\dot{P}_r^{Ok}$ were estimated. Transmissions and radiances from all contributions are combined independently for each radiometer.

Measured FOV Patterns

FOV patterns were measured, in spherical polar coordinates, using frequency-locked transmitters as the signal sources, and were digitally recorded on ground support equipment computers. Far-field ranges were selected instead of near-field or compact ranges, because at the MLS frequencies, the cost of test reflectors, precision translation stages, and equipment to phase-lock receivers to transmitters was prohibitive. Moreover, calculations indicated that atmospheric attenuation was acceptably small and stable, except in the case of R3, for which available transmitter power limited the range to $0.8D^2/\lambda$ instead of the usual $2D^2/\lambda$. Comparisons of R2 patterns on the two ranges showed that errors in the R3 FOV due to phase front curvature could be modeled in the error budget, due to the -15 dB taper of aperture fields. Feed patterns were measured in both subassembly and radiometer configurations to verify proper antenna illumination, alignment sensitivity and aperture spillover levels. These patterns were analyzed to derive Level 1 FOV parameters, while complete FOV patterns (through the antenna) were generated for producing the Level 2 coefficients. Since the atmospheric signals are unpolarized (except from high altitudes in B1), copolarized and cross-polarized patterns were added in power before integrating azimuthal cuts over the horizontal direction.

Complete FOV patterns were measured at 10 scan angles and ~five frequencies within each of bands 1–5 (atmospheric moisture variability precluded patterns in B6, whose performance was extrapolated from B5).

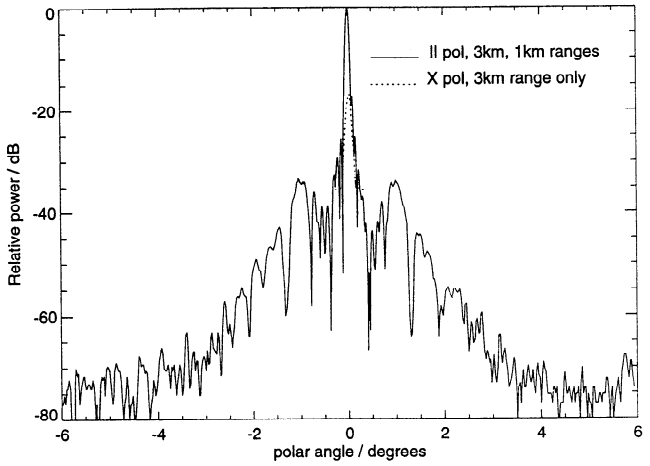

Figure 15. B4 limb vertical FOV pattern, representing a single cut in the domain Ω_A.

Measurements were made at azimuth intervals of 22.5°, and with improved azimuth resolution near features of special interest such as large sidelobes, caustics predicted by the GTD model, and spillover past the secondary reflector, in order to verify predictions of the analytical models. Polar angle resolution varied from 0.01°, in the far sidelobes, to HPBW/70 on the main lobe. The ensuing random errors, combined with systematic variations due to range equipment, transmitted power drift and varying temperature fields, and gravity loads on the MLS, give < 3.5% scatter in HPBW over all patterns measured. Combining this with estimates of launch shift and thermal deformation gives the total uncertainties in Table 5.

FOV boresight directions (dFOV) for B1–B4 were measured to 15 arcsec accuracy, relative to an alignment cube on the MLS, using a theodolite in conjunction with the measured FOV patterns. A 4 arcsec accuracy in knowledge of relative dFOV coincidence (vertical) between any two radiometers was obtained with near-simultaneous pattern measurements using two transmitters.

Figure 15 shows the FOV pattern of B4 in the limb vertical plane, combined from patterns measured on 3 km and 1 km far-field ranges. Since the limb radiance variation is significant only in the vertical direction over much less than the ±6° domain treated in Level 2 processing, measured FOVS were collapsed into the vertical plane, (i.e. integrated over the horizontal direction), to provide one-dimensional FOV functions for the Level 2 forward model.

Small dependences of FOV pattern on scan angle and frequency within the bands are within the measurement uncertainties. For the large (> 100 K) signals in B1 and B4–B6 the upper limit on the effect of variations with scan position and frequency is 0.5% for the spectrally varying component of atmospheric signals. For the weak ClO signal in B2 and B3 the peak-to-peak scatter due to FOV uncertainty provided a prelaunch upper bound of 0.05 K for the uncertainty in calculation of the spectrally varying component of the signal. This was reduced to 0.03 K following results obtained during spacecraft roll maneuvers in flight.

Refinement of FOV Calibration From in-Orbit Data

dFOV knowledge relative to a spacecraft reference. MLS FOV boresight direction (dFOV) knowledge was refined soon after launch by comparing measured radiances in B1 with those calculated from the forward model. An offset of 0.129°, attributed to launch shift or angular uncertainty between MLS and UARS alignment cubes, was found and corrected.

Antenna views of space radiances during yaw and roll maneuvers. Another early refinement to prelaunch FOV calibration was adjustment of radiances $\dot{P}_r^{Sk}$ and $\dot{P}_r^{SL}$ in (17) to make band-averaged radiances at the highest-altitude MMIF match the Planck function values for space radiance. Most of this adjustment occurred in the assumed effective brightness of UARS seen by MLS primary reflector spillover, reduced from an excessive worst-case assumption of 350 K to between 100 K and 150 K. Adjustments were validated using radiances measured during special scans to the antenna 'home' position (tangent height > 250 km) and during ~ 1 orbit of observation with MLS FOV elevated above the Earth's limb by rolling the UARS spacecraft 5° and 20° from its nominal attitude.

Figure 16 shows differences in spectra measured at the top and bottom of the scan (1.8° excursion) during the roll maneuvers. Quadratic functions, fit across the passband of each radiometer, vary by ≤ 0.03 K within any band (and within the combined B2–B3). The 0.04 K excursion across R2 has the same shape for both roll angles, indicating no frequency dependent spillover, but for R3 a difference of 0.05 K, varying linearly with IF frequency, remains after subtracting the two curves. This may arise from incomplete knowledge of sideband ratio and/or far-sidelobe level and is the subject of future work. Weighting the fits with measured rather than theoretical standard deviations produces insignificant differences in fit coefficients. Using radiances from observations in the subsequent orbit (at -5° roll) for the average Earth contribution to $\dot{P}_r^{SL}$, incident on the antenna over [5°, 20°] at +5° roll, we infer upper bounds on the average sidelobe power in this solid angle: -61 dB for B1, -74 dB for B2,B3,B4, and -68 dB for B5 and B6. The upper bound for B2,B3,B4 agrees with the measured FOV (Figure 15).

Comparison of ozone profiles retrieved from R2 and R3. Ozone values retrieved using prelaunch calibration data for R3 exceeded those for R2 by as much as 15%. Three calibration parameters which could cause this discrepancy are sideband ratio, antenna transmission, and dFOV coincidence for R2–R3.

Plausible adjustments to sideband ratio and antenna transmission reduce this discrepancy by only a few percent; in particular, the prelaunch values of R3 baffle transmissions, and the concomitant reflector spillover

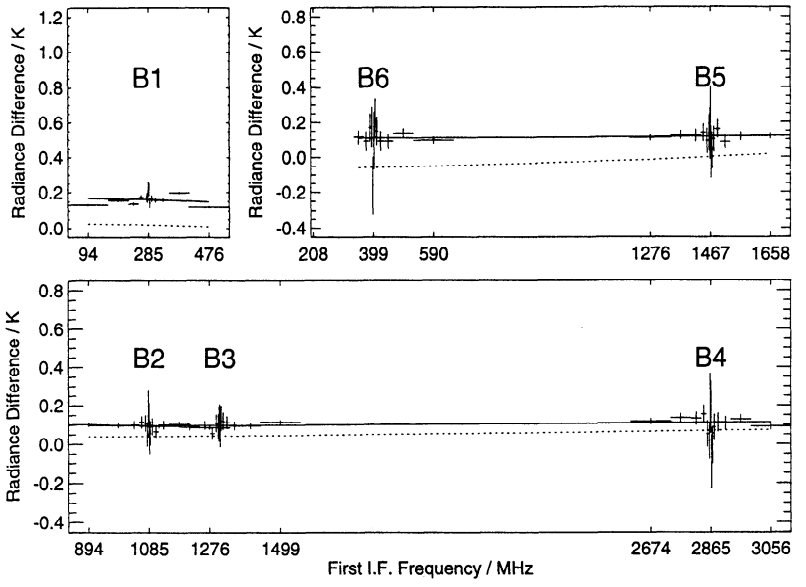

Figure 16. Spectra of radiance differences across the full MLS scan range, obtained during 5° and 20° roll maneuvers. Pluses are differences of calibrated radiances between top and bottom of the scan ($\sim 1.8°$); horizontal extents are nominal channel bandwidths, and vertical extents are theoretical rms radiometric noise. A slowly varying spectral component is indicated by the solid curves, which are quadratic fits. Dashed curves were obtained from the 9 MMAFs at 20° roll.

losses, were replaced by those of R2. This is justified because the front-end optics design of R3 is like that of R2 (differing only due to frequency scaling and polarization), and because its feed pattern characterization was less complete than for R2. Also, an overly conservative estimate of −42 dB for the noise floor of R3 FOV patterns was replaced by −50 dB; that is, more information lay in the prelaunch FOV than had been previously budgeted; hence η_3^{AA} could be increased accordingly. This adjustment perturbed the previous matching of Planck space radiance, discussed above, but the residual spectrally flat offsets are removed by Level 2 processing and therefore have been initially ignored.

Table 6 summarizes Level 1 FOV calibration parameters after in-flight refinement of optical transmission η_3^k and $\dot{P}_r^{SA}$ (all bands); further steps to reconcile R2 and R3 ozone have led us to examine possible deviations from prelaunch values of dFOV coincidence. Initial results of scanning the FOV across the Moon, described next, give a dFOV offset between R2 and R3 which

Table 6. Antenna Transmission and Radiation Offsets for Each MLS Radiometer, After in-Flight Refinement

	R1	R2	R3
Transmission ρ_r^A	0.9923	0.989	0.992
Scattering	0.999	0.993	0.994
Edge diffraction	0.977	0.998	0.998
Primary spillover	0.954	0.985	0.985
Transmission η_r^A	0.931	0.976	0.977
Offset $\dot{P}_r^{SA}$	88.4 K	122.8 K	95.6 K
Offset $\dot{P}_r^{OA}$	252.3 K	256.2 K	251.3 K

$\dot{P}_r^{OA}$ is calculated from orbital averages of $\dot{P}_r^{Ok}$, ranging from 203 K to 313 K in flight and combined for all reflectors using equation (18).

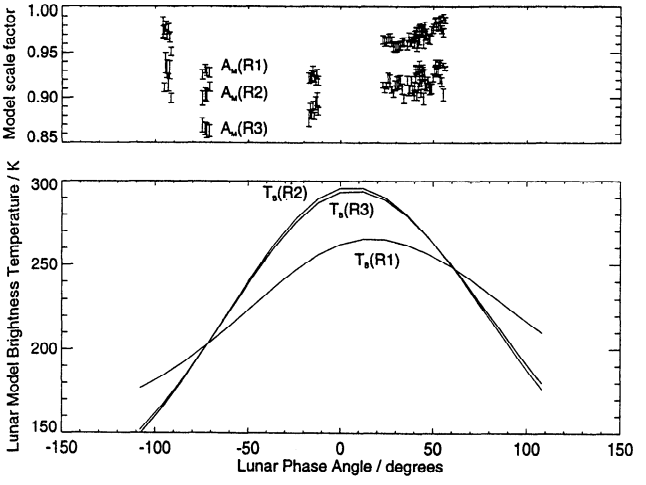

Figure 17. Lunar disk average radiance (bottom panel) and MLS-inferred model scale factor (top panel) versus phase angle. Curves in the bottom panel are brightness temperatures from the lunar model [*Keihm*, 1982], calculated at the three MLS radiometer center frequencies. For this panel, brightness temperatures at lunar phase intervals of 12° have been averaged over both polarizations, then over the lunar disk. However, the MLS antenna has sufficient resolution to permit in-flight calibration of antenna gain and pointing. Error bars, in the top panel, are $\pm 1\sigma$ of model scale factors A_M, inferred from MLS observations during all Moon scans for R1, R2, and at phases of $[-71°, -75°]$ and $[40°, 44°]$ during the 18-month lifetime of R3.

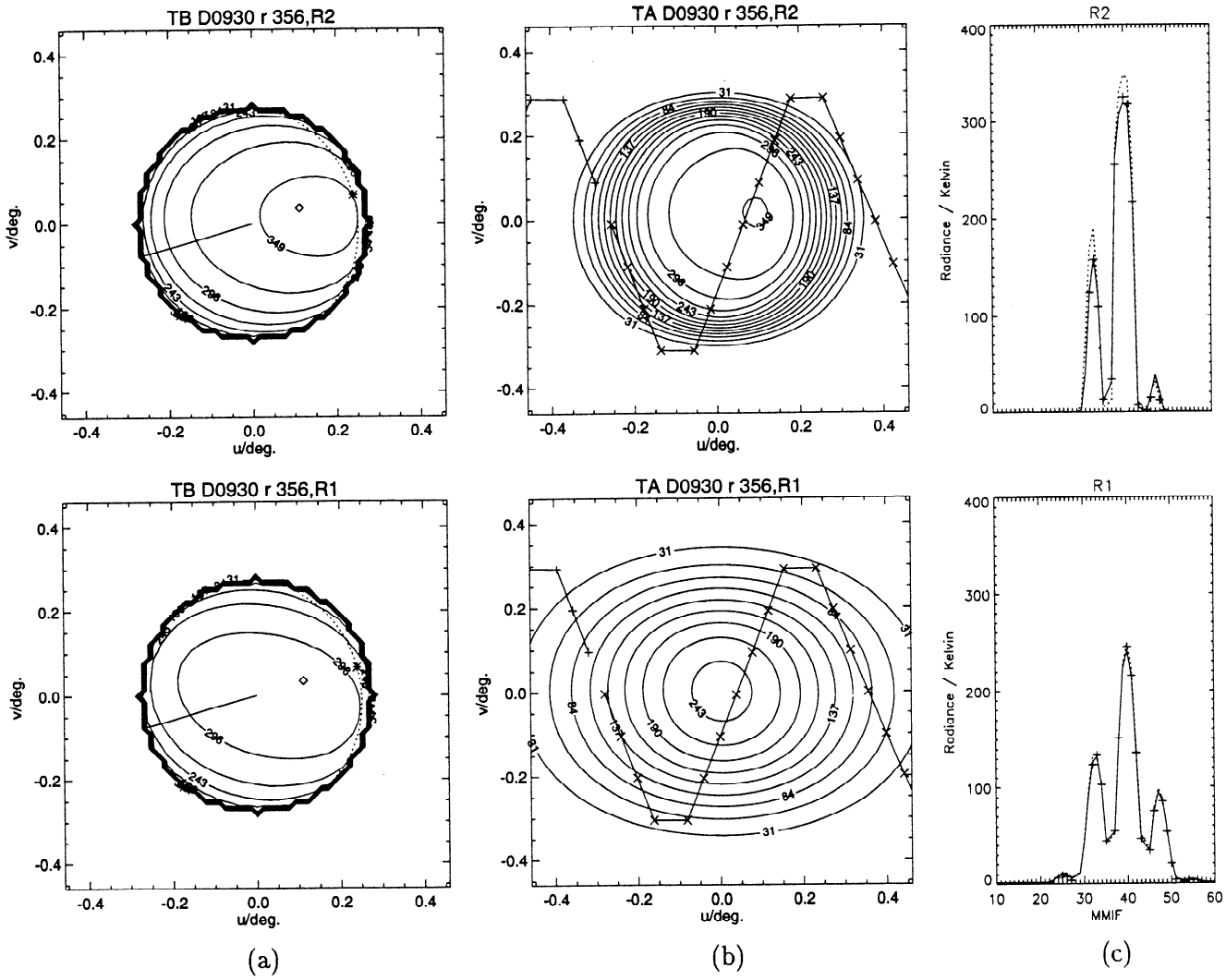

Figure 18. Example of FOV scan through Moon: (a) model radiance incident on the MLS antenna, showing polarization dependence and model angular resolution; (b) convolved limb radiance with scan pattern; (c) radiance time series before (dashed) and after (solid) iterative solution for dFOV and model scale factor A_M.

agrees, within its estimated uncertainty, with the value needed to make R2 and R3 ozone profiles agree [*Froidevaux et al.*, this issue].

Estimation of dFOV coincidence from Moon in the FOV. The envelope of MLS FOV over its scan range intercepts the Moon approximately 17 days per year. To date, the MLS scan pattern has been altered for $\sim 1/7$ of each of 6–12 orbits on seven of these days, letting the Moon drift through the FOV at controlled scan angles well above the atmosphere. Measured radiances were compared to radiances predicted from an Apollo-based lunar microwave model [*Keihm*, 1982], that were convolved with the two-dimensional measured FOVs, swept over the face of the Moon during the ~1.7-s integration time. Figure 17 shows model brightnesses, averaged over the lunar disk, for all lunar phases sampled to date. One can relate measured radiances to the model map and its gradient by two pointing angles and a scaling factor A_M. To first order, deviation of A_M from unity is indistinguishable from an error in η_r^A. These three parameters are estimated by minimizing the sum of squared radiance residuals for the ~30 MMIFs in each Moon crossing.

Figure 18 shows Moon model radiance maps before and after convolution with the MLS FOV. The special scan pattern shown was tailored to minimize the *a priori* variance of retrieved vertical pointing, given the uncertainty in UARS ephemeris predictions and the unavoidable 'horizontal' drift due to orbital motion. The end (right-hand side) panels of Figure 18 superimpose measured radiances on model values before and after the retrieval, showing the high signal-to-noise ratio of this technique.

To combine all Moon scan events, we modified the algorithm to retrieve all three A_M and the two R1 pointing angles separately for each event, but one (event independent) set of pointing offsets from R1 to R2 and R1 to R3 boresights. This formalized the notion that

Table 7. Coincidence of Vertical FOV Boresight Direction Between Radiometers

	R2–R1 , deg		R3–R1 , deg	
	$d\epsilon$	3σ	$d\epsilon$	3σ
Prelaunch	+0.006	0.0016	−0.001	0.0021
from Moon scans	−0.003	0.0006	+0.0013	0.0036

The angle ϵ, from the orbit plane normal vector to the MLS boresight, increases with decreasing tangent height; hence for R2–R1, $d\epsilon < 0$ means that R2 dFOV is pointed higher in the atmosphere than R1.

large ($\sim 0.07°$) variations in absolute dFOV (from a spacecraft reference to each radiometer's boresight), attributed to uncertainties in both the Moon model and the spacecraft attitude, still cancel in the subtraction of retrieved angles to obtain the dFOV differences between R1 and the other two radiometers.

Figure 17 shows the ensemble of values retrieved for scaling factor A_M from all Moon scans to date. The value of A_M retrieved for R1 differs from unity by an amount consistent with the Moon model's accuracy [*Keihm*, 1982], estimated for observations by other space-borne radiometers at 32–90 GHz [*Bennett et al.*, 1992]. The larger deviations for R2 and R3 may suggest some residual error in far sidelobe level of the FOV functions.

Table 7 compares prelaunch dFOV coincidence with results from the Moon observations. Uncertainties for the Moon-scan method are less than those estimated for the prelaunch calibration for R2-R1 but not for R3, which operated only on the first two days of Moon scanning, before the scan pattern in Figure 18 had been developed. The change in dFOV between R1 and R2 is statistically significant, and the inferred dFOV between R2 and R3 agrees to $\sim 50\%$ with the offset required to account for the discrepancy between R2 and R3 ozone retrievals [*Froidevaux et al.*, this issue].

FOV Calibration Summary

Prelaunch calibration provided nearly all FOV parameters and functions required for flight data processing. Exceptions are absolute pointing error (due to launch shift between MLS and UARS references), radiance offset (due to incomplete knowledge of background stray radiance), and dFOV coincidence between R2 and R1 FOVs (attributed to launch shift). In-flight data have been used to refine parameters in all three areas, with efforts to resolve the residual R2-R3 ozone differences continuing.

Table 8 summarizes systematic uncertainties in FOV. As with radiometric and spectral calibrations, scaling uncertainties have been separated from radiance offsets, which are removable by Level 2 processing. Table 8 also contains estimates of uncertainties in the detailed FOV patterns; these were used for the error analyses in the works of Froidevaux *et al.* [this issue], and Fishbein *et al.* [this issue].

Engineering Data Calibration

The majority of MLS engineering data is taken to monitor the operation, health, and safety of the instrument. A subset of these data, in particular calibration target temperature, enters directly into radiometric calibration.

Engineering data are calibrated in a manner similar to radiances; voltages are measured by V/F converters which cycle through 32 input sources each MMAF (~65 s), two of which are references (0 V, and the output of a stable ~6.2 V reference). Resistances of temperature sensors are measured by recording their voltage drop when passing ~1 mA derived from a low-drift current source. Each current source is multiplexed through 16 data sources in ~32 s, two of which are resistance references. With this system it is required that the reference voltages and resistances be stable for the duration of the mission, drifts in signal-chain offsets and gains, and excitation current levels, being removed by the frequent periodic calibrations. Traceability to external standards is achieved by calibrating the engineering data acquisition subsystems using traceable secondary standards, by using stable, calibrated onboard references, and by using platinum resistance device (PRD) temperature sensors calibrated by the vendor against traceable standards for calibration-critical temperature measurements. There are 10 temperature sensors in the internal calibration target, each monitored twice per MMAF using different current sources, signal chains, and V/F converters. There has been no divergence of inferred temperatures via the separately calibrated signal paths at levels above a few hundredths of a Kelvin. Further evidence of the long-term stability of engineering data calibration is provided by the ensemble of ~150 voltages, currents, and temperatures monitored routinely each MMAF. Trend plots of these data after 3 years of operation reveal no significant drift in any parameter with the exception of the bias for the 183-GHz mixer which failed after just over 18 months of in-orbit operation. Engineering data are acquired through seven

Table 8. Summary of FOV Uncertainties

	B1	B2–4	B5–6
Level 1 scaling uncertainty (3σ)	2.4%	1.4%	1.5%
HPBW uncertainty (3σ)	0.006°	0.003°	0.005°
HPBW stability over 1 UARS yaw cycle	0.0004°	0.0004°	0.0004°
Exponent α describing end-to-end accuracy of FOV measurement	0.979	0.964	0.943

Scaling uncertainties from all FOV sources mentioned in the text have been combined into this contribution to total calibration scaling uncertainty. The 3σ uncertainty in linearity of the FOV measurements is described by an exponent α which relates a worst-case measured FOV G' to the actual FOV G: $G'(\theta,\phi) = G^{\alpha}(\theta,\phi)$.

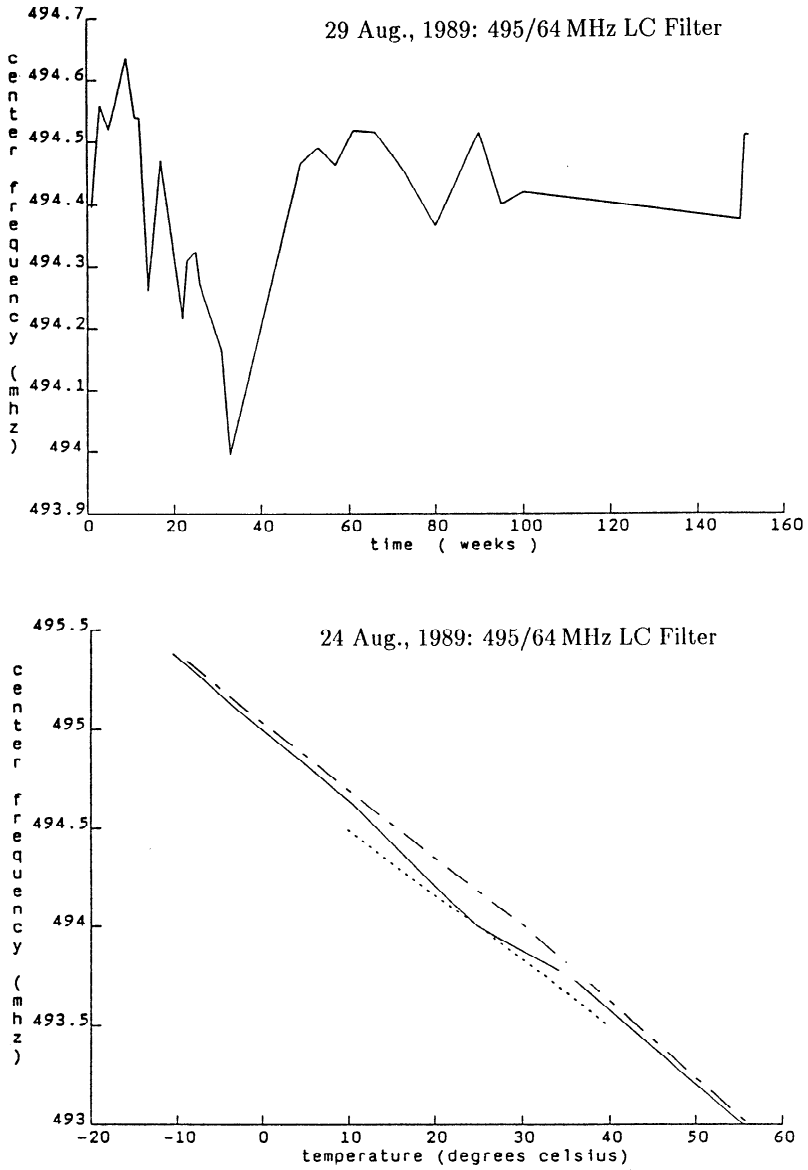

Figure 19. Life test data for a 64-MHz-wide LC filter. Top panel is measured center frequency at 25°C over a 3-year period. Bottom panel shows temperature dependence of center frequency measured at ~1-year intervals. In-flight operating temperature range for the filter bank spectrometers has been 15° to 21°C during the first 3 years of operation. Temperature dependence of channel center frequency and width is approximately proportional to channel width for both the LC and SAW filters used in MLS spectrometers.

signal chains, each with independent signal conditioning paths, references, and digitizers. Values of the reference counts for all signal chains exhibit no trends, confirming that the signal chains and internal references have remained extremely stable.

Stability

Accurate prelaunch calibrations are only of value for the duration of the mission if long-term stability is such that drifts in instrument characteristics over the mission lifetime do not impart significant additional error. The radiometer signal chains are self-calibrating by using the switching mirror to remove the effects of electronic gain variations and offset drifts. The antenna and radiometer optics were tested for mechanical stability by measuring FOV patterns before and after vibration testing. All frequency sources within the instrument are phase locked to a highly stable (1 part in 10^7 over the duration of the mission) quartz master oscillator. Long-term stability of the spectrometer filters was verified by performing life tests at elevated operating temperatures and by vibration tests.

Figure 19 shows the results of life and temperature testing on a 64-MHz-wide LC filter. The life tests were run at elevated temperature (~50°C) for a duration of

approximately 3 years and indicate no significant drift. The bottom panel shows the temperature dependence of channel center frequency over an extended range measured on three occasions approximately one year apart. Similar tests on 2-MHz-wide SAW filter channels indicate both channel drift and temperature dependence to be reduced by a factor of 30 from those shown in Figure 19, in proportion to the filter width. Changes in channel characteristics at these levels have a negligible effect on calibration parameters. Stability of the signal chains is also indicated in Figure 3, which gives examples of the measured gains in two channels of B1, and shows no long-term drift in end-to-end performance of all elements from the switching mirror through to the spectrometer digitizers. All channels are monitored for trends and indicate stability similar to that just described.

Relative sideband ratio was determined to be insensitive to temperature and LO drive levels for the variations expected over mission life. Sensitivity to front-end mixer bias was found to be significant. Mixer DC and RF bias levels are both determined by ground control, allowing compensation for aging of any portion of the bias and LO chains. MLS mixers are operated in flight at their ground test bias levels.

Future Work

Future algorithms will refine spectral baseline handling by generating a daily set of radiance corrections derived from that day's observed radiances for limb views with tangent heights of ~90 km or more. This reduces residual spectral baseline to ~0.03 K and eliminates the ~1 K yaw cycle variation in the offset component. These algorithms will be included in the next release of Level 1 production software.

Further moon scans are planned for additional refinement of R1/R2 dFOV knowledge but may be limited in scope due to desires to limit antenna scan activities in order to prolong instrument operational lifetime.

Preliminary analyses of radiance curves of growth measured in the tropics by B6 when the stratosphere was nearly isothermal have shown that it is possible to retrieve relative sideband ratio for this band, since each sideband saturates at different tangent heights. This work is in progress, as is that for the retrieval of the relative sideband response of B1 from flight data. These data will be included in a future release of Level 2 software.

Conclusions

The rss sums of the 3σ calibration scaling uncertainties listed in Tables 3 and 4 indicate scaling uncertainties in calibrated limb radiance in bands B1 through B3 of up to ~2.6%, ~3.4% in B4, and ~6% in B5. Simultaneously measured O_3 profiles from bands B4 and B6 differed by up to ~15% using prelaunch calibration data. Errors of this magnitude are consistent with the R3 antenna transmission and boresight (dFOV) uncertainties and uncertainties in relative sideband response in B6 similar to those given for B5.

Random uncertainties in Table 3 for individual limb integrations are very close to the performance expected from radiometer noise alone, with negligible contribution from instrument gain and offset drifts and from noise on the in-flight calibration measurements.

UARS MLS has demonstrated the viability of microwave limb sounding from low Earth orbit, having provided 3 years of nearly continuous data, and a further year of lower duty cycle (~50%) measurements limited primarily by the reduction in available spacecraft power.

We have shown that double sideband, total-power operation of microwave radiometers is suitable for demanding remote sensing tasks and that such systems can be adequately calibrated to provide high quality data, as further demonstrated by results given in companion papers [*Fishbein et al,* this issue; *Froidevaux et al,* this issue; *Lahoz et al,* this issue; *Waters et al,* this issue] describing validation of the major MLS data products.

Appendix A

The following table is an alphabetical list of symbols used in this document, together with the equation of their first occurrence, and a brief definition.

Appendix B

Our objective here is to relate the power received by a coherent (heterodyne) radiometer to the temperature of a blackbody which completely fills its FOV. By "coherent" we mean that electromagnetic radiation is coupled to the radiometer in a manner which preserves its phase; this places constraints on the modes which are received and influences the effective area of the aperture which "collects" the radiation. Let $I_\nu(\theta,\phi)$ be the intensity ($\mathrm{W\,Hz^{-1}\,m^{-2}\,sr^{-1}}$) of unpolarized radiation incident upon a collecting aperture from direction (θ,ϕ). The power in frequency interval $d\nu$ delivered through the aperture to a single-polarization radiometer can then be written

$$dP_\nu = \frac{1}{2}\,d\nu \int_\Omega I_\nu(\theta,\phi)\,A_e(\theta,\phi)\,d\Omega \ , \qquad \text{(B1)}$$

where $A_e(\theta,\phi)$ is the effective collecting area, the factor of $\frac{1}{2}$ is due the radiometer accepting only one polarization, and the integral is over solid angle Ω.

A general expression for $\int A_e(\theta,\phi)\,d\Omega$ is derived from considerations of a thermodynamic equilibrium situation. Let the collecting aperture be immersed in a cavity of blackbody radiation and let thermal equilibrium be established at temperature T between the blackbody and the radiation in the transmission line which matches the aperture to the radiometer. If V is volume of the cavity, then the blackbody radiation intensity is

Symbol	Dimension	Equation	Description
$A_e(\theta,\phi)$	m^2	B1	effective collecting area of antenna in direction (θ,ϕ)
c	$m\,s^{-1}$	B2	speed of light in vacuum
C_i	counts	10	digitized output from channel i
C_i^O	counts	10	digitizer offset for channel i
$\langle E\rangle_T$	J	B2	average energy in a single mode at temperature T
$F(\nu)$		3	normalized frequency response
$G(\nu,\theta,\phi)$		3	angular gain function
$G^M(\nu,\theta,\phi)$		4	angular gain function at switching mirror
$G_r^A(\theta,\phi)$		7	antenna angular gain function for radiometer r
g_i	Counts K^{-1}	10	gain of channel i
Δg	Counts K^{-1}	15	noise on interpolated gain
h	Js	1	Planck's constant
$\dot{I}_\nu(\theta,\phi)$	$K\,sr^{-1}$	3	radiant power per unit bandwidth and solid angle
k	JK^{-1}	1	Boltzmann's constant
L	m	B3	line length
N_1	Hz^{-1}	B3	number of modes per unit frequency
$N_3(\nu)$	Hz^{-1}	B2	number of modes per unit frequency interval in a three-dimensional cavity
$\overset{*}{P}_i^X$	W	8	calculated signal power in channel i for view X
$\dot{P}_i^X$	W	3	signal power in channel i for view X
$\dot{P}_\nu$	K (= $W\,Hz^{-1}$)	1	radiant power per unit bandwidth
$\Delta\dot{P}$	K (= $W\,Hz^{-1}$)	14	uncertainty in $\dot{P}$
dP_ν	$W\,Hz^{-1}$	B1	power in a single polarization in frequency interval $d\nu$
dP_ν^{BB}	$W\,Hz^{-1}$	B5	power per unit frequency interval emitted by a blackbody
dP_ν^T	$W\,Hz^{-1}$	B3	thermal equilibrium power in a transmission line within the frequency interval $d\nu$
ΔR	K	15	noise on interpolated space reference
T	K	1	temperature
T_x	K	14	radiometric brightness temperature of object x
T_{sys}	K	14	radiometer noise temperature
v	$m\,s^{-1}$	B3	propagation velocity within a transmission line
V	m^3	B2	volume of cavity
η^X		5	fractional optical transmission (efficiency) integrated over solid angle for aperture X
λ	m	B8	radiation wavelength
ν	Hz	1	radiation frequency
ν_r	Hz		radiometer center (first LO) frequency
ϕ	rad	3	elevation angle
ρ^A		9	antenna transmission due to ohmic loss
ρ_r^k		17	reflectivity of reflector k for radiometer r
θ	rad	3	azimuth angle
Ω_A	sr	8	angle over which antenna pattern is measured
Ω_{MX}	sr	4	solid angle defined by baffles
$d\Omega$	sr	3	element of solid angle $[d\Omega = \sin(\theta)\,d\theta\,d\phi]$

given by

$$I_\nu^{BB} = \left\{\frac{\mathcal{N}_3(\nu)\,\langle E\rangle_T}{V}\right\}\left\{\frac{c}{4\pi}\right\}. \quad \text{(B2)}$$

The first factor in braces in (B2) is the average energy per unit volume; the second is the conversion to isotropic radiation intensity with c being the speed of light. $\mathcal{N}_3(\nu)$ is the number of modes per unit frequency interval in the three-dimensional cavity, and $\langle E\rangle_T = h\nu\,/\,\{\exp(h\nu/kT) - 1\}$ is the average energy in a single mode at temperature T and frequency ν [e.g., *Feynman et al.*, 1963, vol. 3, chap 4]. The thermal equilibrium power in the transmission line within the frequency interval $d\nu$ which is moving towards the aperture is

$$dP_\nu^T = \left\{\frac{\mathcal{N}_1 \langle E\rangle_T}{L}\right\}\left\{\frac{v}{2}\right\} d\nu \ , \qquad \text{(B3)}$$

where L is the line length. The first factor in braces in (B3) is the average energy per unit length in the line and the second converts it to power moving toward the aperture where v is propagation speed in the line (in equilibrium, half the power moves toward the aperture and half moves away from it). $\mathcal{N}_1$ is the number of modes per unit frequency and $\langle E\rangle_T$ is the same as in (B2) since the average energy per mode at thermal equilibrium depends only on temperature and frequency. In thermal equilibrium the transmission line power moving toward the aperture will equal that collected from the radiation field by the aperture and delivered to the line. Setting (B3) equal to (B1), and using (B2) for $I_\nu(\theta,\phi)$ which can be taken outside the integral since the blackbody radiation is isotropic, leads to

$$\int_\Omega A_e(\theta,\phi)\, d\Omega = 4\pi \frac{v}{c} \frac{\mathcal{N}_1/L}{\mathcal{N}_3(\nu)/V} \ . \qquad \text{(B4)}$$

Using (B2) and (B4) in (B1) gives, for a blackbody source,

$$\frac{dP_\nu^{BB}}{d\nu} = \langle E\rangle_T \frac{\mathcal{N}_1}{L}\frac{v}{2} \ . \qquad \text{(B5)}$$

The significant difference between (B5) and (B3) is that (B3) requires the transmission line to be in thermal equilibrium with the blackbody, whereas (B5) does not. Heterodyne radiometers, such as in MLS, use a "single-mode" transmission line for which $\mathcal{N}_1 = 2L/v$, so (B5) becomes

$$\frac{dP_\nu^{BB}}{d\nu} = \langle E\rangle_T \ , \qquad \text{(B6)}$$

$$\frac{dP_\nu^{BB}}{d\nu} = h\nu \,/\, \{\exp(h\nu/kT) - 1\} \ , \qquad \text{(B7)}$$

which is the relation between the blackbody temperature and the power per unit frequency received by a heterodyne radiometer whose FOV is completely filled by the blackbody.

Although it is not needed for the above derivation, the number of modes per unit frequency for a three-dimensional blackbody cavity of volume V is $\mathcal{N}_3(\nu) = 8\pi\nu^2 V/c^3$. When this and the expression given above for $\mathcal{N}_1$ are used in (B4), we obtain

$$\int_\Omega A_e(\theta,\phi)\, d\Omega = c^2/\nu^2 = \lambda^2 \ , \qquad \text{(B8)}$$

where λ is wavelength of the radiation. By invoking detailed balancing at thermal equilibrium (the principle that equilibrium must apply to *each* frequency, direction, and polarization [e.g., *Reif*, 1965, section 9-15]), and using the preceding arguments leading to equation (B4), the effective aperture area for collecting radiation from direction (θ,ϕ) is shown to be given by

$$A_e(\theta,\phi) = \frac{\lambda^2}{4\pi} G(\theta,\phi) \ , \qquad \text{(B9)}$$

where $G(\theta,\phi)$ is the aperture's angular "gain." (If unit power is delivered to the aperture by the line, the amount radiated within solid angle $d\Omega$ in direction (θ,ϕ) is $G(\theta,\phi)\, d\Omega/4\pi$). Note that $\int G(\theta,\phi)\, d\Omega = 4\pi$, as follows from using (B9) in (B8). Combining (B1) and (B9) gives

$$dP_\nu = d\nu \frac{1}{4\pi}\int_\Omega \dot{I}_\nu(\theta,\phi)\, G(\theta,\phi)\, d\Omega \ , \qquad \text{(B10)}$$

where

$$\dot{I}_\nu = \frac{1}{2}\lambda^2 I_\nu \ . \qquad \text{(B11)}$$

Equation (B10) is applied several places in this paper. Equations (B8), (B9), and (B10) describe general properties of coherent radiometer systems. The derivations given here are based on notes from classes taught by A.H. Barrett and D.H. Staelin at the Massachusetts Institute of Technology.

Acknowledgments. We gratefully acknowledge contributions by many colleagues, especially M.A. Frerking for measurements of calibration target emissivity; J.C. Hardy for construction of the sideband measurement apparatus; R.A. Lay for monitoring and daily operation of the instrument and his assistance with the analysis of in-flight data; M. Loo for his considerable assistance with the fabrication and testing of both ground and flight electronic subsystems; V.S. Perun for writing the ground test and analysis software; E.F. Fishbein for adding sequential estimation to the lunar pointing calibration and, with L. Froidevaux, for comments on the manuscript; H.M. Pickett and W.G. Read for useful discussions; and B.J. Connor for his thorough review of the submitted manuscript. This work above was performed at the Jet Propulsion Laboratory, California Institute of Technology, under contract with the National Aeronautics and Space Administration, and at Heriot-Watt University, Edinburgh, Scotland, under sponsorship of the NERC.

References

Barath, F.T., et al., The Upper Atmosphere Research Satellite Microwave Limb Sounder instrument, *J. Geophys. Res., 98*, 10,751–10,762, 1993.

Bennet, C. L., *COBE* differential microwave radiometers: Calibration techniques, *Astrophys. J., 391*, 466–482, 1992.

Born, M. and Wolf, E., *Principles of Optics*, Pergamon, New York, 1980.

Feynman, R. P., R. B. Leighton, and M. Sands, *The Feynman Lectures on Physics*, Addison-Wesley, New York, 1963.

Fishbein, E.F., et al., Validation of UARS Microwave Limb Sounder temperature and pressure measurements, *J. Geophys. Res., this issue.*

Froidevaux, L., et al., Validation of UARS Microwave Limb Sounder ozone measurements, *J. Geophys. Res., this issue*, [1996].

Hilton, H.E., A 10-MHz Analog-to-Digital Converter with 110-dB Linearity, Hewlett-Packard Journal, October 1993.

Janssen, M. (Ed.), *Atmospheric Remote Sensing by Microwave Radiometry*, John Wiley, New York, 1993.

Jarnot, R.F., and R.E. Cofield, Microwave Limb Sounder instrument calibration report, *JPL Internal Doc. D-9393*, Jet Propulsion Lab., Pasadena, Calif., 1991.

Keihm, S. J., Interpretation of the lunar microwave brightness temperature spectrum: Feasibility of orbital heat flow mapping, *Icarus, 60*, 568–589, 1984.

Lahoz, W.A., et al., Validation of UARS Microwave Limb Sounder 183 GHz H_2O measurements, *J. Geophys. Res., this issue.*

Marx, E., and T. Vorburger, Direct and inverse problems for light scattered by rough surfaces, *App. Opt.*, 29, 3613–3626, 1990.

Njoku, E., Passive microwave remote sensing of the earth from space — A review, *Proc. IEEE, 70*, 728–750, 1982.

Reif, F., *Fundamentals of Statistical and Thermal Physics*, McGraw-Hill, New York, 1965.

Ruze, J., Antenna tolerance theory—A review, *Proc. IEEE, 54*, 633–640, 1966.

Robinson, F.N.H., *Noise and Fluctuations in Electronics Devices and Circuits*, Clarendon, Oxford, 1974.

Schanda, E., Passive microwave sensing, in *Remote Sensing for Environmental Sciences*, edited by E. Schanda, pp. 229–240, Springer-Verlag, New York, 1979.

Staelin, D., Passive remote sensing at microwave wavelengths, *Proc. IEEE, 57*, 427–439, 1969.

Ulaby, F.T., et al., *Microwave Remote Sensing Active and Passive*, vol. I, *Microwave Remote Sensing Fundamentals and Radiometry*, Addison-Wesley, Reading, Mass., 1981.

Ulaby, F.T., et al., *Microwave Remote Sensing Active and Passive*, vol. III, *From Theory to Applications*, Addison-Wesley, Reading, Mass., 1986.

Waters, J.W., Microwave limb sounding, *Atmospheric Remote Sensing by Microwave Radiometry*, edited by M.A. Janssen, chap. 8, John Wiley, New York, 1993.

Waters, J.W., et al., Validation of UARS Microwave Limb sounder ClO measurements, *J. Geophys. Res., this issue.*

R. E. Cofield, D. A. Flower, R. F. Jarnot and J. W. Waters, Jet Propulsion Laboratory, MS 183-701, 4800 Oak Grove Drive, Pasadena, CA 91109-8099

G. E. Peckham, Physics Department, Heriot-Watt University, Riccarton, Currie, Edinburgh ED14 4AS, Scotland

(Received July 5, 1995; revised December 6, 1995; accepted December 6, 1995.)